Plasmonics (2025) 20:2895–2919
https://doi.org/10.1007/s11468-024-02520-0

RESEARCH

Terahertz Plasmonic Biosensor Leveraging Ag-Au-Graphene Heterostructures for Quantitative Hemoglobin Analysis with Machine Learning Algorithms for Performance Optimization

Jacob Wekalao[1] · Ngaira Mandela[2] · Costable Lefu[3] · Obed Apochi[4] · Calistus Wamalwa[5] · Wesley Langat[6]

Received: 14 August 2024 / Accepted: 28 August 2024 / Published online: 4 September 2024

Abstract

This investigation presents the design, simulation, and performance analysis of a terahertz-based biosensor for hemoglobin detection. The sensor architecture incorporates a synergistic combination of graphene, gold, and silver metasurfaces in a hierarchical resonator structure. Extensive parametric analysis was conducted to optimize the sensor's performance characteristics. The optimized sensor demonstrates high sensitivity, achieving up to 1000 GHzRIU^{-1}, with a figure of merit of 3.289 RIU^{-1}. Experimental results indicate effective detection of hemoglobin concentrations ranging from 10 to 40 g/L, corresponding to refractive indices between 1.34 and 1.43. Electromagnetic field distribution analysis exemplifies peak absorption at 0.65 THz. Furthermore, the sensor's potential for binary encoding applications was evaluated with remarkable performance. Machine learning optimization, employing a decision tree regressor, demonstrates an optimal R^2 score of 100% across various parameter combinations, suggesting potential for the development of accurate sensing systems. The proposed sensor design represents a significant advancement in terahertz biosensing technology, with implications for enhanced medical diagnostics and biomedical research applications.

Keywords Optical sensing · Binary encoding · Machine learning optimization · Plasmonic resonance · Electromagnetic field confinement · Sensor

Introduction

Biosensors have become a crucial focus in medical diagnostics and health monitoring research [1]. These devices integrate biological recognition elements with physicochemical detectors to analyze and quantify biomolecular levels across different sample types [2]. Various types of biosensors have been developed for different applications, each tailored with unique advantages and applications [3]. Electrochemical biosensors are widely used in detecting electrical changes generated when biomolecules interacts with the sensor's components [4]. Optical biosensors rely on alterations in properties like absorbance or fluorescence to identify presence of biomolecules [5]. Piezoelectric biosensors detect shifts in mass on their surface caused by analyte binding [6]. The identification components employed in these biosensors are pivotal for their accuracy and responsiveness [7]. Antibodies are extensively employed in immunosensors due to their exceptional specificity towards analytes [8]. Recent advancements in biosensors for biomedical applications have concentrated on enhancing their effectiveness and ease of

✉ Jacob Wekalao
jacob.phdfs2303@nfsu.ac.in

1 School of Engineering and Technology, National Forensic Sciences University, Gandhinagar, Gujarat 382007, India

2 School of Digital Forensics and Cyber Security, National Forensic Sciences University, Gandhinagar, Gujarat 382007, India

3 School of Pharmacy, National Forensic Sciences University, Gandhinagar, Gujarat 382007, India

4 School of Behavioural Sciences, National Forensic Sciences University, Gandhinagar, Gujarat 382007, India

5 Department of Physics, University of Embu, P.O. BOX 6-60100, Embu, Kenya

6 Department of Environmental Studies, Delhi University, Benito Juarez Marg, South Campus, South Moti Bagh, Delhi, New Delhi 110021, India

use. By integrating nanomaterials like graphene, carbon nanotubes, and metal nanoparticles, sensor sensitivity and specificity have been significantly improved [9]. Additionally, there is a rising emphasis on creating point-of-care devices—portable biosensors that are simple to use and enable quick analyte detection across different environments, ranging from clinics to remote locations [10].

Several studies highlight advancements in biosensors for blood analysis. Li et al. demonstrated an extensive overview of electrochemical biosensors with specific focus on advancements in electrode materials and sensing techniques for hemoglobin detection [11]. Rasheed et al. on the other hand presented an optical biosensors, exploring diverse optical sensing mechanisms and their applicability in point-of-care cases [10]. Ji et al. demonstrated an optical biosensor using aptamers to detect hemoglobin, incorporating graphene oxide and gold nanoparticles [12]. Yazdanpanah et al. presented a review on advancements in electrochemical biosensors for hemoglobin detection, focusing on their suitability for biomedical applications [13]. Wu et al. introduced an innovative electrochemical biosensor for highly sensitive detection of low-concentration proteins such as hemoglobin [14].

Metasurfaces are materials designed to manipulate and control electromagnetic waves at scales smaller than the wavelength [15, 16]. Unlike traditional optical components that depend on bulky lenses and mirrors, metasurface function by arranging nanostructures on a flat surface, allowing room for exceptional control over light propagation [17]. These surfaces consist of arrays of subwavelength elements—typically metallic or dielectric nanostructures—organized in specific patterns [18, 19]. By modifying the size, shape, and orientation of these nanostructures, metasurfaces can precisely influence the phase, amplitude, and polarization of incoming light [20]. This capability enables a variety of transformative optical functions, such as focusing light into finely resolved spots, shaping wavefronts to create complex optical patterns, and directing light along unconventional paths [21]. Metasurfaces are employed in numerous fields, including telecommunications, imaging, sensing, and quantum optics. They provide compact and versatile alternatives to traditional optical components, facilitating the miniaturization of devices and systems while improving their performance and functionality [22, 23].

Graphene consists of a single layer of carbon atoms arranged in a two-dimensional honeycomb lattice. It is renowned for its outstanding properties: exceptional electrical conductivity, mechanical strength, and thermal conductivity [24]. Since its discovery in 2004, graphene has sparked widespread interest across multiple fields [25]. One of graphene's notable attributes is its high electrical conductivity, marked by impressive electron mobility, making it an outstanding conductor of electricity [26]. This feature is pivotal for advancing faster and more efficient electronic devices [27]. Despite its thin structure, graphene exhibits remarkable mechanical strength, boasting a tensile strength more than 100 times greater than steel [28]. This exceptional strength-to-weight ratio positions it as an ideal material for durable. Graphene also excels in thermal conductivity, effectively dissipating heat [29]. This property is particularly advantageous in applications requiring efficient thermal management, such as in electronics [30]. Furthermore, its flexibility allows for integration into various substrates, facilitating the development of bendable electronics and wearable technology [31].

In this study, we present a biosensor design employing graphene-Au-Ag metasurface for the quantitative detection of hemoglobin via terahertz (THz) spectroscopy. This integrated approach leverages the unique electronic properties of graphene in conjunction with the localized surface plasmon resonance (LSPR) effects of Au and Ag nanostructures to enhance the sensitivity and specificity of hemoglobin detection in the THz regime. The manuscript is structured as follows: "Design and Modeling" exemplifies the biosensor design parameters and the finite element method (FEM) simulation protocol implemented in COMSOL Multiphysics. "Results and Discussion" delineates the simulation results and subsequent analysis of hemoglobin detection employing the proposed biosensor. Finally, "Machine Learning Optimization with Decision Tree Regressor" presents the machine learning-based optimization of the sensor design, using decision tree algorithms to enhance its performance.

Design and Modeling

A highly sensitive optical sensor has been developed employing a graphene, silver, and gold based metasurfaces deposited on a SiO_2 substrate. The sensor's architecture is elegantly simple yet effective, as depicted in Fig. 1a–c, which provides structural, top, and front views, respectively. At the heart of the design is a hierarchical resonator structure engineered to enhance electromagnetic field confinement and light-matter interactions. The sensor's central element is an inner square resonator (ISR) with a precise side length of 1.2 µm, which can be fabricated with a tolerance of ±5 nm using electron-beam lithography. This ISR is surrounded by four rectangular resonators, each measuring 4 µm (±10 nm) by 0.5 µm (±5 nm). These components are integrated into a larger square resonator design measuring 8.5 µm (±20 nm) on each side. This multi-resonator configuration is designed to create multiple plasmonic hotspots, significantly enhancing the local electromagnetic field and improving the sensor's detection limit.

The substrate structure is characterized by a total length of 11 µm (±25 nm), with key features delineated by dimensions of 1.7 µm (±10 nm) and 1.6 µm (±10 nm). The choice

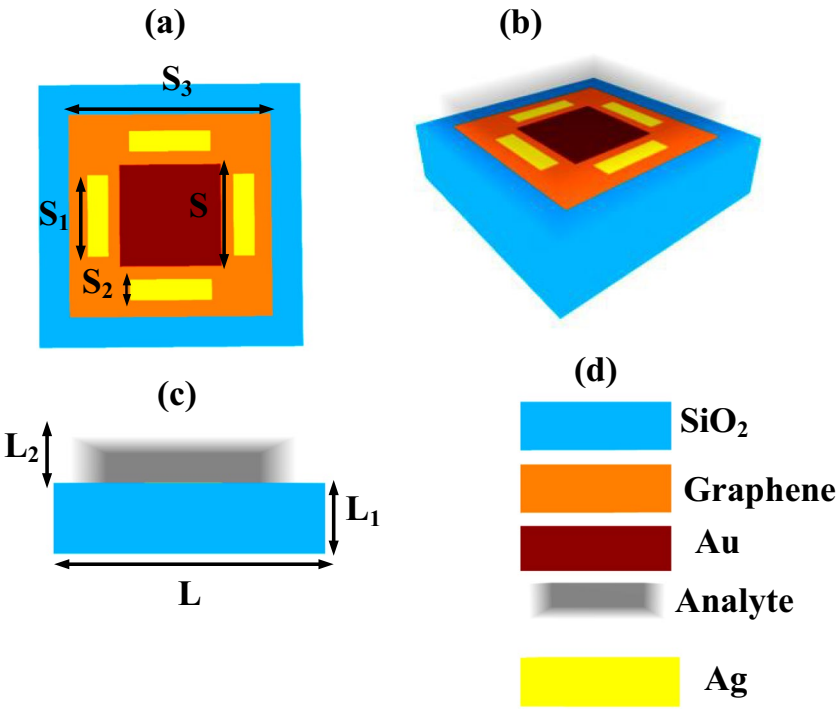

Fig. 1 Schematic representation of a conceptual sensor employing a graphene metasurface. The illustration provides multiple perspectives: **a** top view, **b** three-dimensional view, **c** front view, and **d** cross-sectional view detailing the sensor's material composition and design elements

of SiO_2 as the substrate material is deliberate, selected for its low optical loss in the target wavelength range of 400–2000 nm. This SiO_2 layer is thermally grown on a silicon wafer to ensure optimal performance. The dimensions and tight tolerances specified in the design highlight the high level of control required in the fabrication process.

The fabrication of the high-sensitivity optical sensor begins with a silicon wafer, upon which a layer of SiO_2 is grown. This substrate is selected for its low optical loss in the 400–2000 nm wavelength range. Electron beam lithography (EBL) is then employed to pattern a graphene-gold metasurface onto the SiO_2 surface. The design incorporates an inner square resonator with a precise side length of 1.2 µm ± 5 nm, surrounded by four rectangular resonators, each measuring 4 µm (±10 nm) by 0.5 µm (±5 nm). These components are integrated into a larger square resonator design measuring 8.5 µm (±20 nm). Following the patterning process, graphene and gold layers are deposited onto the substrate using appropriate techniques to ensure uniform coverage and adherence to the SiO_2 surface. After fabrication, the sensor undergoes rigorous characterization and testing. Scanning electron microscopy (SEM) is utilized to verify the dimensions and structural integrity of the fabricated resonators. Optical measurements are conducted to evaluate the sensor's performance in terms of electromagnetic field confinement and light-matter interactions. Throughout the process, adjustments are made to optimize fabrication parameters such as dimensions and deposition techniques, with the aim of achieving the desired sensitivity and detection limits.

Factors Determining Sensor Performance

Sensor performance evaluation is a complex process involving multiple interconnected parameters, each providing unique understanding into the sensor's capabilities. At the core of this evaluation is sensitivity, which measures how responsive the sensor is to changes in the input. It is expressed as a change in frequency per unit change in refractive index, with higher sensitivity indicating the ability to detect smaller changes [32].

$$S = \frac{\Delta f}{\Delta n} \tag{1}$$

The figure of merit combines sensitivity with the sharpness of the sensor's response, providing a comprehensive measure of overall performance. A higher figure of merit suggests better performance, as it represents high sensitivity with a narrow response peak. This parameter is particularly useful when comparing sensors with different operational principles [33–35].

$$\text{FOM} = \frac{S}{\text{FWHM}} \tag{2}$$

The quality factor, often referred to as Q factor, is a dimensionless parameter describing how underdamped a resonator is. It indicates the rate of energy loss relative to the stored energy of the resonator. In practical terms, a higher Q factor results in sharper resonance peaks and potentially higher sensitivity [36–39].

$$Q = \frac{fr}{\text{FWHM}} \tag{3}$$

Signal-to-noise ratio is crucial for determining the clarity of the sensor's output. It indicates how easily the sensor can distinguish the actual signal from background noise, which is particularly important in environments with high electromagnetic interference or when detecting very small changes [40–43].

$$\text{SNR} = \frac{\Delta f}{\text{FWHM}} \tag{4}$$

Dynamic range indicates the span of input values over which the sensor can operate effectively. A larger dynamic range means the sensor can measure a wider span of input values accurately, which is important in applications where the input can vary greatly, such as in environmental monitoring [44–47].

$$\text{DR} = \frac{f_r}{\sqrt{\text{FWHM}}} \tag{5}$$

Detection accuracy is inversely related to the width of the senso's response peak. Higher accuracy suggests that the sensor can precisely pinpoint the exact value of the input, which is crucial in applications requiring high precision measurements [48–51].

$$\text{DA} = \frac{1}{\text{FWHM}} \tag{6}$$

The detection limit represents the smallest change in input that can be detected by the sensor. A lower detection limit is generally better, indicating the sensor can detect very small changes in the measured quantity.

$$\text{DL} = \left(\frac{\Delta n}{1.5}\right) \times \left(\frac{\text{FWHM}}{\Delta f}\right)^{1.25} \tag{7}$$

Sensor resolution combines sensitivity with the detection limit, giving an overall measure of the sensor's ability to distinguish small changes in the input. A higher resolution indicates better performance in detecting minute variations.

$$\text{SR} = S \times \text{DL} \tag{8}$$

The uncertainty coefficient relates to the error in the sensor's measurements. It takes into account the magnitude of the frequency change and the width of the response peak. A lower uncertainty coefficient indicates more reliable measurements.

$$\text{Uncertainty}(X) = \frac{2(\Delta f)^{0.75}(\text{FWHM})^{0.25}}{9} \tag{9}$$

These parameters are interconnected and often involve trade-offs. For instance, increasing sensitivity come at the cost of a reduced dynamic range, or improving the detection limit require sacrificing some aspect of the signal-to-noise ratio. A very high Q factor result in a sensor that is slower to respond to changes. In practice, the relative importance of these parameters depends on the specific application of the sensor. Environmental monitoring prioritizes a wide dynamic range, while medical diagnostics require a low detection limit. Real-time control systems emphasize a high signal-to-noise ratio and fast response. Understanding these parameters and their relationships allows engineers and researchers to optimize sensor designs for specific applications, balancing various performance aspects to achieve the best overall functionality for the intended use. This comprehensive approach to sensor evaluation ensures that the resulting devices are well-suited to their target applications, whether in biosensing, environmental monitoring, chemical detection, or other fields requiring precise and reliable measurements.

The relationship between reflectance, angle of incidence, graphene potential, and conductivity is defined by Eqs. 10–15 [52]

$$r(\omega,\theta_i) = \frac{\cos\theta_i \prod_{00}(\omega,\theta_i)}{2ick^2 + \omega\cos\theta_i \prod_{00}(\omega,\theta_i)} \tag{10}$$

$$\sigma_{\parallel}(\omega,\text{k}) = X = -i\frac{\omega}{4\pi\hbar\, k^2}\prod_{00}(\omega,k) \tag{11}$$

$$r(\omega,\theta_i) = \frac{2\pi\cos\theta_i \sigma_{\parallel}(\omega,k)}{c + 2\pi\cos\theta_i \sigma_{\parallel}(\omega,k)} \tag{12}$$

$$R(\omega,\theta_i) = \left|r(\omega,\theta_i)\right|^2 \tag{13}$$

$$R(\omega,\theta_i) = \frac{4\pi^2\cos^2\theta_i\left[Re^2X + Im^2X\right]}{\left[c + 2\pi\cos\theta_i ReX\right]^2 + 4\pi^2\cos^2\theta_i Im^2X} \tag{14}$$

$$R(\omega) = R(\omega,0) = \frac{4\pi^2\left[Re^2\sigma(\omega) + Im^2\sigma(\omega)\right]}{[c + 2\pi Re\sigma(\omega)]^2 + 4\pi^2 Im^2\sigma(\omega)} \tag{15}$$

Table 1 Refractive indices of various hemoglobin compounds

RIs	n_1	n_2	n_3	n_4
Value (RIU)	3.4	3.6	3.9	4.3
Concentration	10	20	30	40

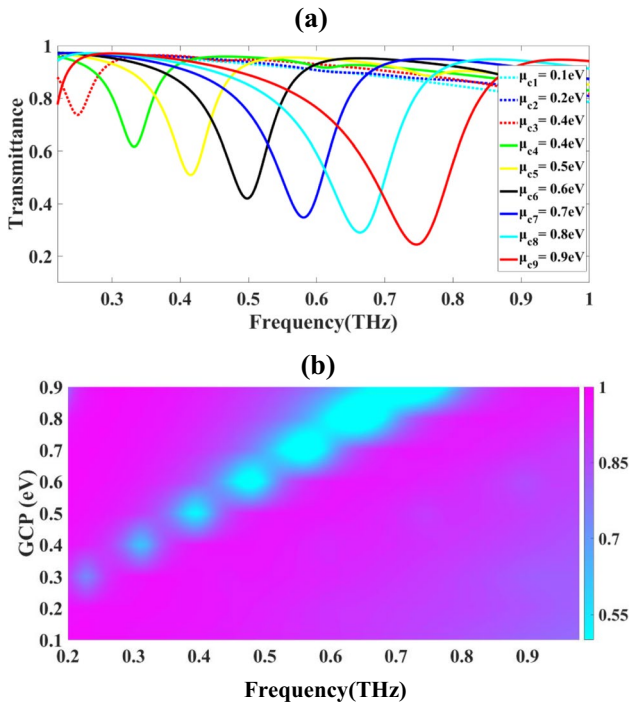

Fig. 2 The influence of GCP variations on the sensor's transmission response

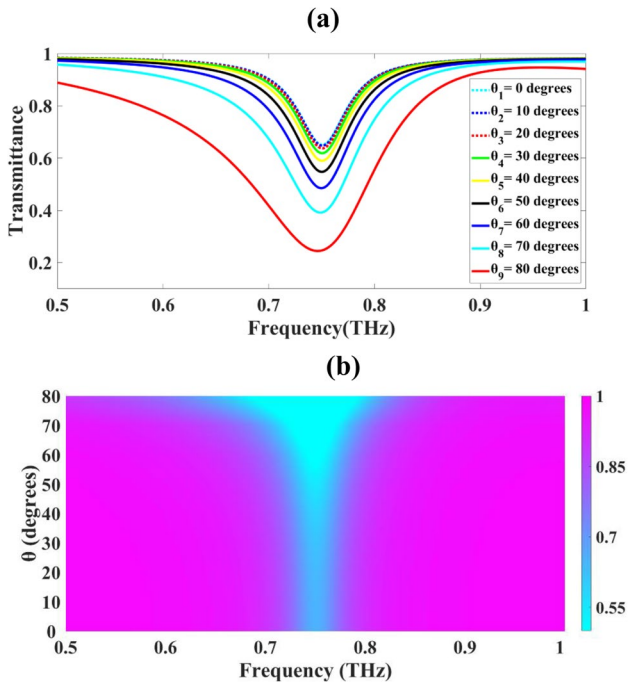

Fig. 3 Transmittance response as a function of varying incidence angles, illustrated through line and color plots

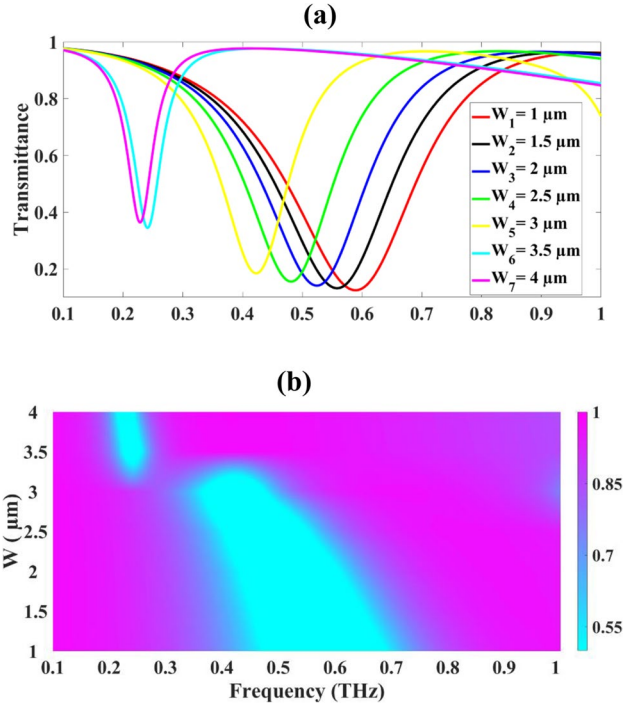

Fig. 4 The impact of varying the width of rectangular resonators on the transmittance response, depicted through line and color plots

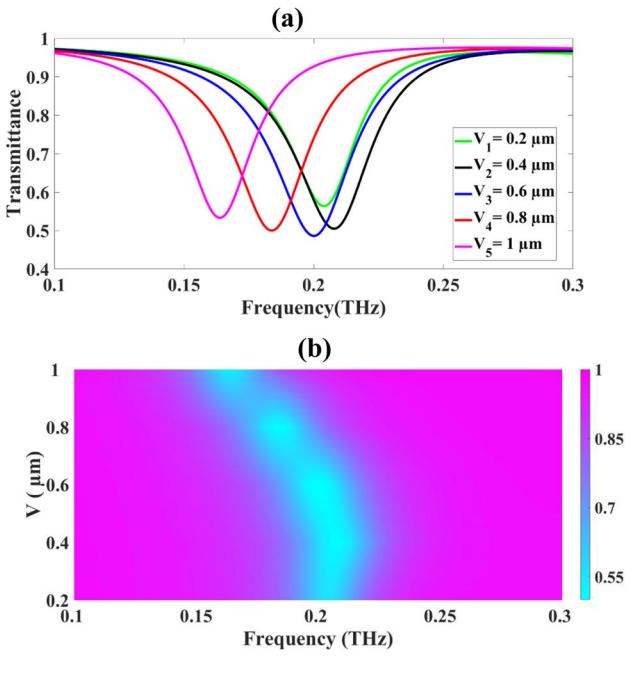

Fig. 5 The impact of varying the height of rectangular resonators on the transmittance response

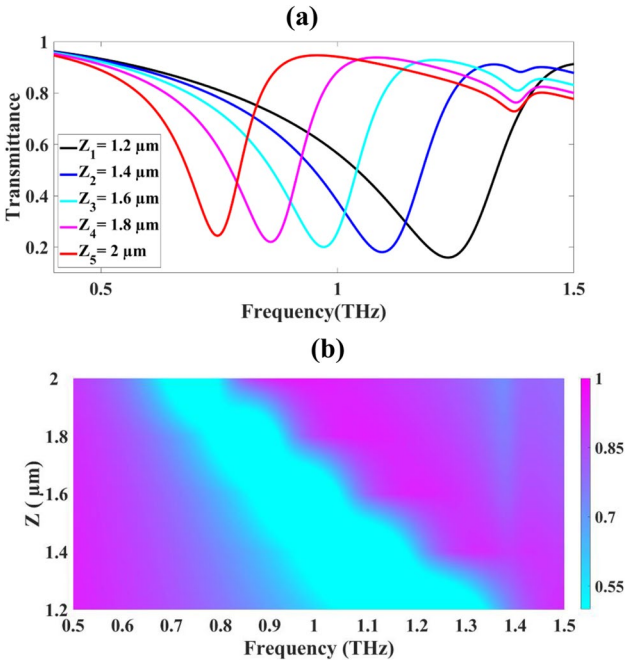

Fig. 6 The impact of varying the inner square resonator on the transmittance response

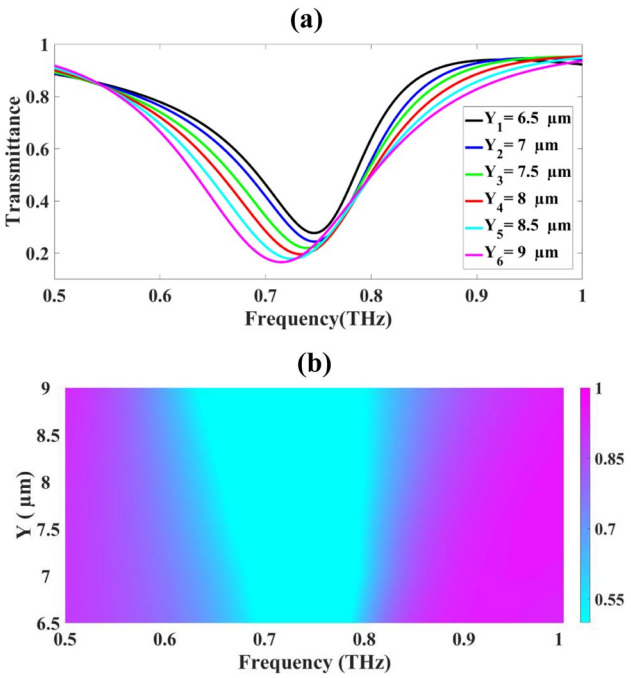

Fig. 7 The impact of varying the outer square resonator on the transmittance response, depicted through line and color plots

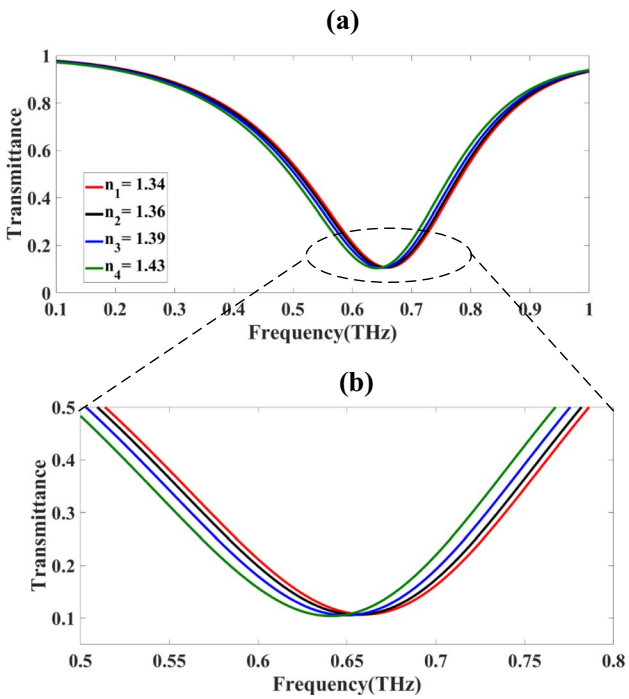

Fig. 8 The variation in transmittance response corresponding to changes in the refractive index of hemoglobin, resulting from alterations in concentration

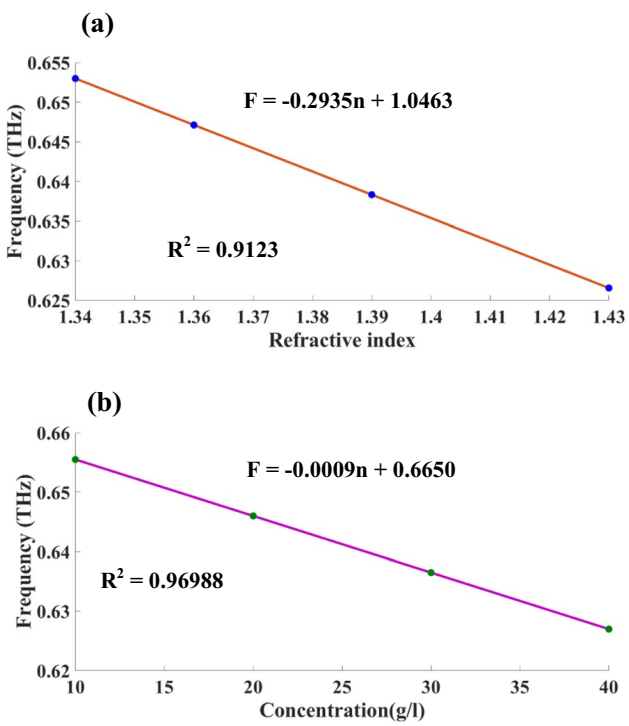

Fig. 9 depicts the curve fitting for the correlation between resonance frequency and refractive index (*n*) (**a**), as well as concentration (**b**)

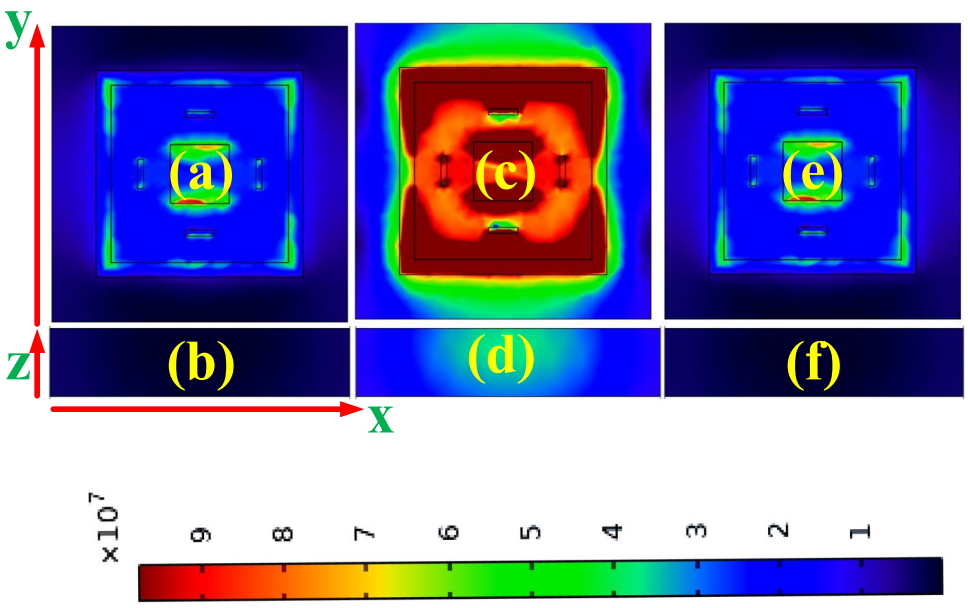

Fig. 10 Depicts how the electric field intensity (EFI) is distributed across various terahertz frequencies for the proposed design

The impedance and transmittance of the proposed sensor are defined by [53]

$$Z = \pm\sqrt{\frac{\left(1+s_{11}\right)^2 - s_{21}^2}{\left(1-s_{11}\right)^2 - s_{21}^2}} \tag{16}$$

$$e^{ink_0 d} = \frac{s_{11}}{1 - s_{11}\frac{2-1}{2+1}} \tag{17}$$

$$n = \frac{1}{k_0 d}\left\{\left[\ln e^{ink_0 d}\right)\right]'' + 2m\pi\right\} - i\left[\ln\left(e^{ink_0 d}\right)\right]'\Big] \tag{18}$$

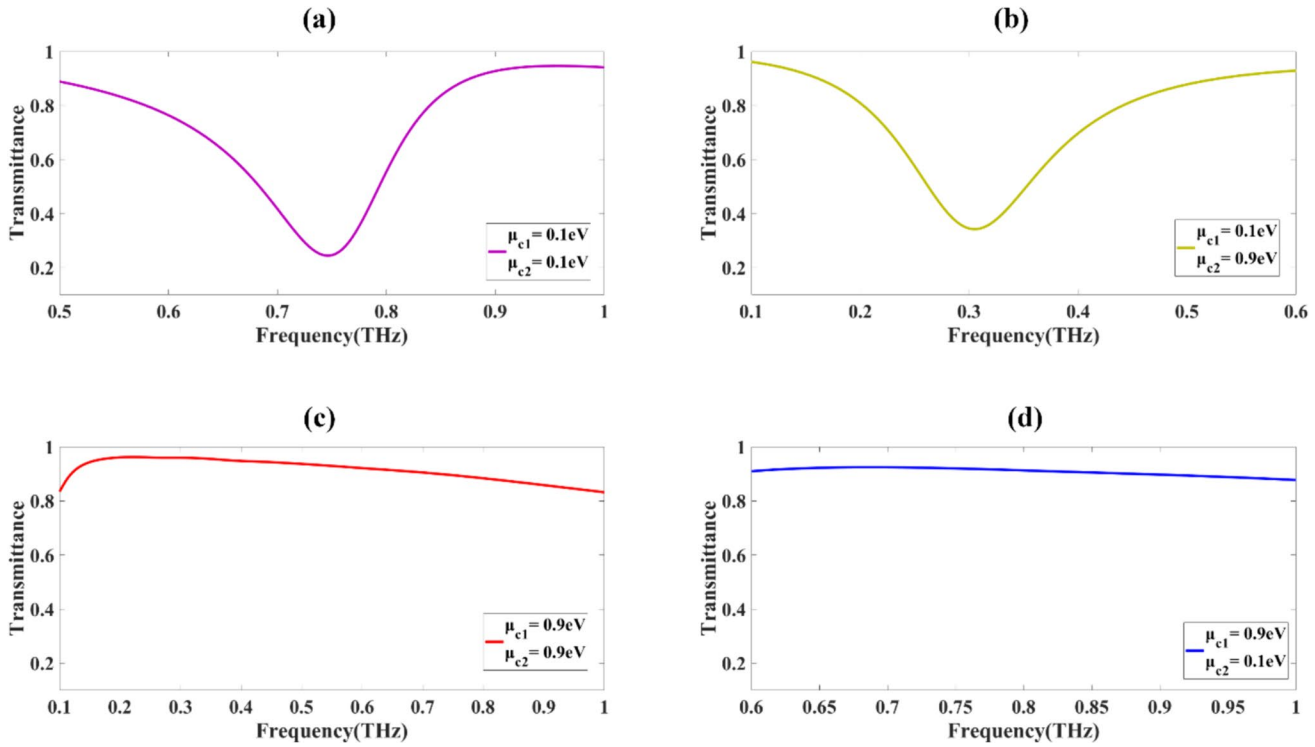

Fig. 11 Binary encoding capabilities of the sensor design

Table 2 The performance metrics of the proposed sensor design

f (THz)	0.66	0.64	0.635	0.63
n (RIU)	1.34	1.36	1.39	1.43
df (THz)		0.02	0.005	0.005
dn (RIU)		0.02	0.03	0.04
S (GHzRIU^{-1})		1000	167	125
FWHM (THz)	0.304	0.304	0.304	0.304
FOM (RIU^{-1})		3.289	0.548	0.411
Q		2.171	2.105	2.089
DL		0.400	3.396	4.527
DR	1.197	1.161	1.152	1.143
SNR		0.066	0.016	0.016
SR		0.400	0.566	0.566
DA	3.289	3.289	3.289	3.289
X		0.009	0.003	0.003

$$\varepsilon = \frac{n}{z} \tag{19}$$

$$\mu = nz \tag{20}$$

$$A(w) = 1 - R(w) - T(w) = 1 - \left|s_{11}\right|^2 - \left|s_{21}\right|^2 \tag{21}$$

Equation 21 is used to determine the transmittance.

In graphene, the Kubo formula provides a quantitative relationship that connects the electrical conductivity (σ) to both the characteristics of the electronic band structure and the various scattering mechanisms that electrons encounter within the material. This relationship is expressed through rigorous mathematical equations, which demonstrates how the conductivity depends on factors such as the density of states, carrier velocities, and the nature of scattering events like impurities, defects, or phonons. These elements collectively define the material's ability to conduct electricity. Some of these equations includes [41]

$$\varepsilon\ (\omega) = 1 + \frac{\sigma_s}{\varepsilon_0 \omega \nabla} \tag{22}$$

$$\sigma_{\text{intra}} = \frac{-je^2 k_B T}{\pi\hbar^2\ (\omega - j2\Gamma)}\left(\frac{\mu_c}{k_B T} + 2\ \ln\left(e^{\frac{\mu_c}{k_B T}} + 1\right)\right) \tag{23}$$

$$\sigma_{\text{inter}} = \frac{-je^2}{4\pi\hbar}\ \ln\left(\frac{2\left|\mu_c\right| - (\omega - j2\Gamma)\hbar}{2\left|\mu_c\right| + (\omega - j2\Gamma)\hbar}\right) \tag{24}$$

$$\sigma_s = \sigma_{\text{intra}} + \sigma_{\text{inter}} \tag{25}$$

The refractive index of silicon dioxide is given by [54]

$$n(\lambda) = \sqrt{1 + \frac{B_1 C}{\lambda^2 - C_1} + \frac{B_2 \lambda^2}{\lambda^2 - C_2} + \frac{B_3 \lambda^2}{\lambda^2 - C_3}} \tag{26}$$

The Drude model [37] is used to explain the relative permittivity of gold.

$$\varepsilon_{\text{Au}} = \varepsilon_\infty - \frac{\omega_D^2}{\omega\left(\omega + j\gamma_D\right)} - \frac{\Delta_\varepsilon \Omega_L^2}{\left(\omega^2 - \Omega_L^2\right) + j\Gamma_L \omega} \tag{27}$$

Hemoglobin, a tetrameric metalloprotein crucial for oxygen transport in erythrocytes, serves as a key biomarker in various medical diagnostics. While spectrophotometric and colorimetric assays remain prevalent, refractive index (RI)-based techniques offer an alternative approach with distinct advantages in hemoglobin quantification [55]. The refractive index, defined as the ratio of the speed of light in vacuo to its velocity in a given medium, provides a measure of a substance's optical density. In hemoglobin detection, variations in RI correlate with changes in the protein's concentration, allowing for quantitative analysis. The methodology for RI-based hemoglobin detection involves several steps. Initially, sample preparation requires isolation or dilution of hemoglobin in an appropriate buffer solution. Subsequently, RI measurement is conducted using refractometers or similar optical instruments to determine the sample's refractive index. Calibration follows, involving the generation of a standard curve using solutions of known hemoglobin concentrations. Finally, quantification is achieved through interpolation of unknown sample concentrations based on the calibration curve. This technique offers several advantages, including non-destructive analysis, high sensitivity to minor

Table 3 Comparative analysis of the proposed sensor with other similar cases

Sensing structure	S	FOM (RIU^{-1})	DL (RIU)	Q	Application
Ref [57]	130 GHz/RIU	4.37	–	179.95	Hemoglobin detection
Ref [58]	7.75,103 nm/RIU	–	–	–	THz sensing
Ref [45]	443 GHz/RIU	2.368	0.063	7.684	Explosive detection
Ref [57]	130 GHz/RIU	4.37	–	179.95	Detection of hemoglobin
Ref [47]	153.85 GHz/RIU	3.98	0.041	8.54	Detection of brain tumor
Ref [59]	107.9 GHz/RIU	3.15	0.45	11.22	Cu^{2+} detection
Proposed sensor	1000 GHz/RIU	3.289	0.400	2.171	Detection of hemoglobin

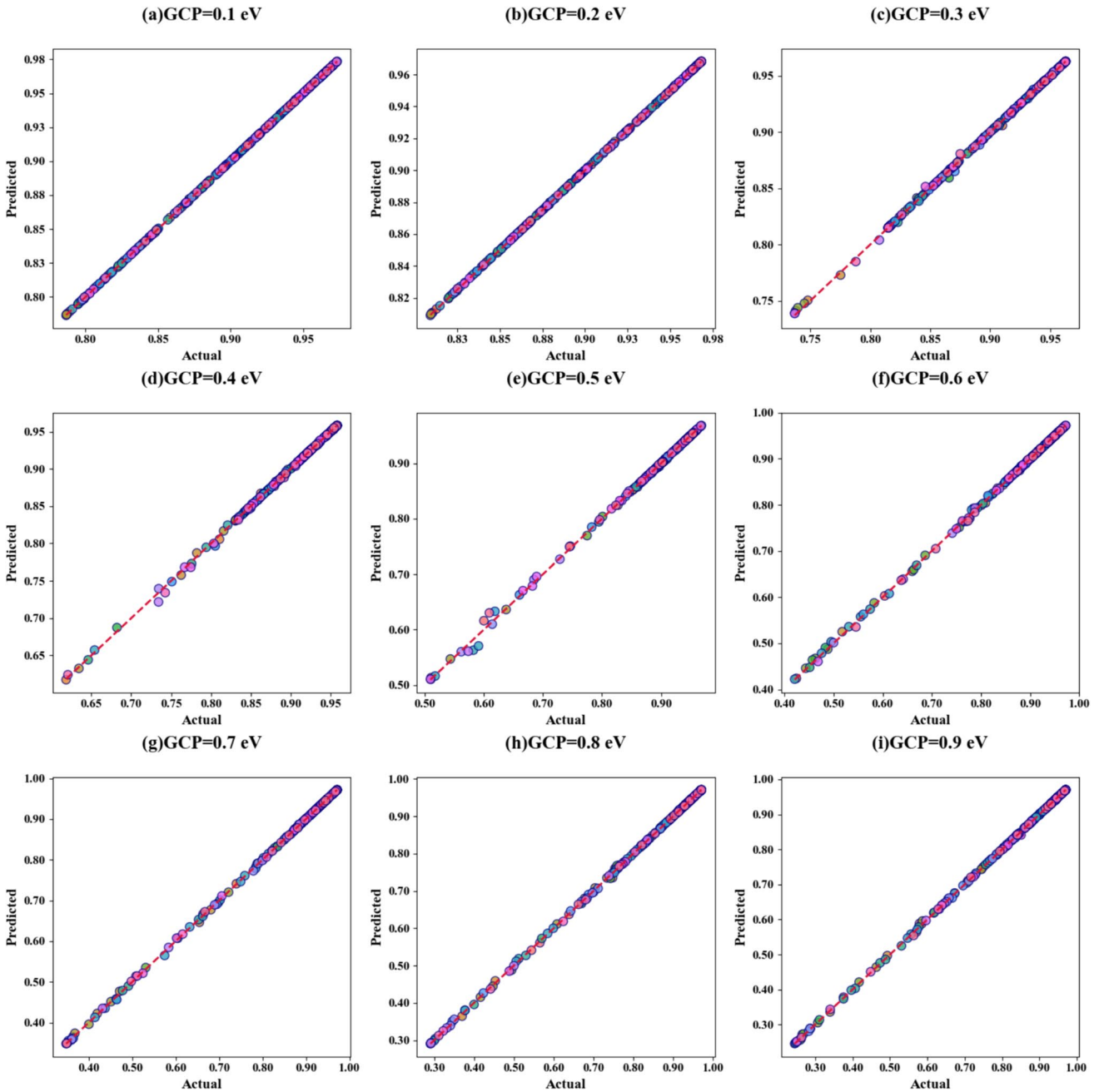

Fig. 12 Scatter plots for GCP variation

concentration changes, and rapid turnaround times. However, it also presents challenges, such as potential interference from other solutes and the need for sophisticated data interpretation algorithms. The RI method's efficacy is influenced by factors including temperature, wavelength of incident light, and sample purity. Careful control of these variables is essential for accurate and reproducible results. Despite its limitations, RI-based hemoglobin detection holds significant potential in clinical diagnostics, biomedical research, and point-of-care testing Table 1.

Results and Discussion

In the simulation of the designs illustrated in Fig. 1 using COMSOL Multiphysics, planar electromagnetic wave propagation along the *z*-axis is employed to generate a frequency spectrum ranging from 0.1 to 1 THz. The computational model incorporates high-resolution tetrahedral meshing techniques to accurately represent the complex geometries and material interactions inherent in the system. Figures 2, 3, 4, 5, 6, 7, 8, 9, 10, and 11 present comprehensive transmittance spectra

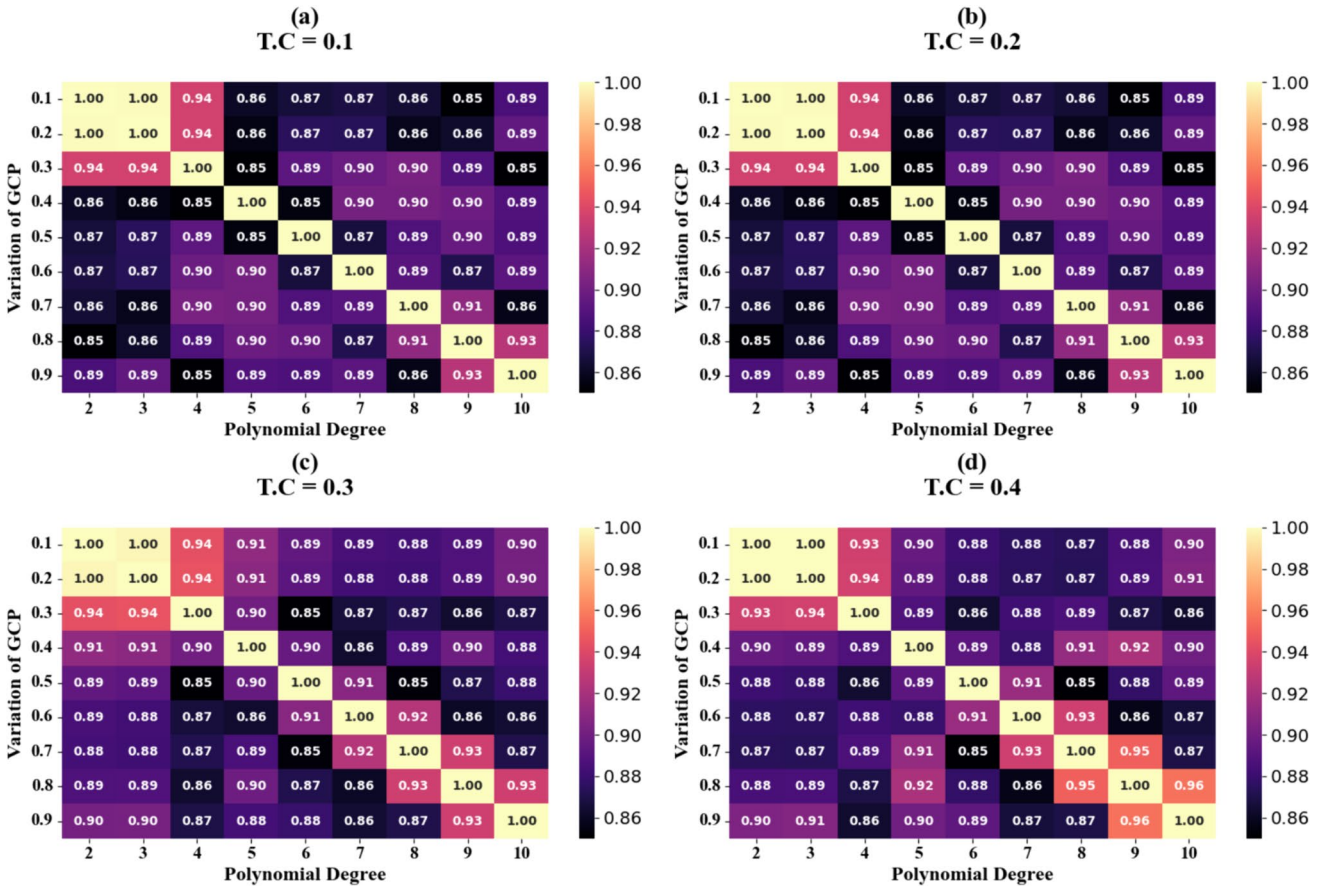

Fig. 13 Heat map plots for GCP variation

that demonstrates the effects of various structural parameters. These parameters include variation of graphene chemical potential (μ_c), resonator dimensions, and electric field strength (E) distributions. The resultant spectra not only validate the achieved transmittance levels but also provide critical insights into the structure-function relationships governing the sensor's performance.

The initial investigation examined the impact of varying graphene chemical potential (GCP) on the transmittance response of the sensor. GCP was systematically varied from 0.1 to 0.9 eV in 0.1 eV increments. Figure 2a, b illustrates the results through line and color plots, respectively. Figure 2a demonstrates an inverse relationship between transmittance and GCP. Notably, at GCP values of 0.1 eV and 0.2 eV, no clear transmittance reduction was observed within the analyzed frequency range, indicating near-perfect transmittance. As GCP increased from 0.5 to 0.9 eV, the observed transmittance drops are 50.89%, 41.97%, 34.77%, 29.03%, and 24.46%, respectively, across 0.35–1 THz. This phenomenon is primarily attributed to enhanced graphene conductivity at higher GCP values, resulting in stronger interactions with incident electromagnetic waves and consequently greater transmittance modulation. Figure 2b presents a color plot demonstrating a rightward shift in transmittance across the selected frequency range as a function of increasing GCP. This visualization highlights the inverse relationship between GCP and transmittance observed in the line plot.

To optimize the structural design, we conducted a parametric study focusing on the angle of incidence and other resonator parameters. We systematically varied the angle of incidence (θ) from 0 to 80° in 10° increments, analyzing its effect on transmittance as depicted in Fig. 3a, b. The observed transmittance values were 65.11%, 64.77%, 63.72%, 61.86%, 58.98%, 54.72%, 48.50%, 39.16%, and 24.46%, corresponding to $\theta = 0°$, 10°, 20°, 30°, 40°, 50°, 60°, 70°, and 80°, respectively.

The color plot in Fig. 3 illustrates an inverse relationship between the angle of incidence and both transmittance and transmission bandwidth. As θ increases, we observe a marked decrease in transmittance and a concomitant widening of the transmission band. This phenomenon suggests that the sensor's angular response becomes more selective at higher angles of incidence, this inverse relationship can be attributed to the increased optical path length and enhanced reflectivity at the interface as the angle of

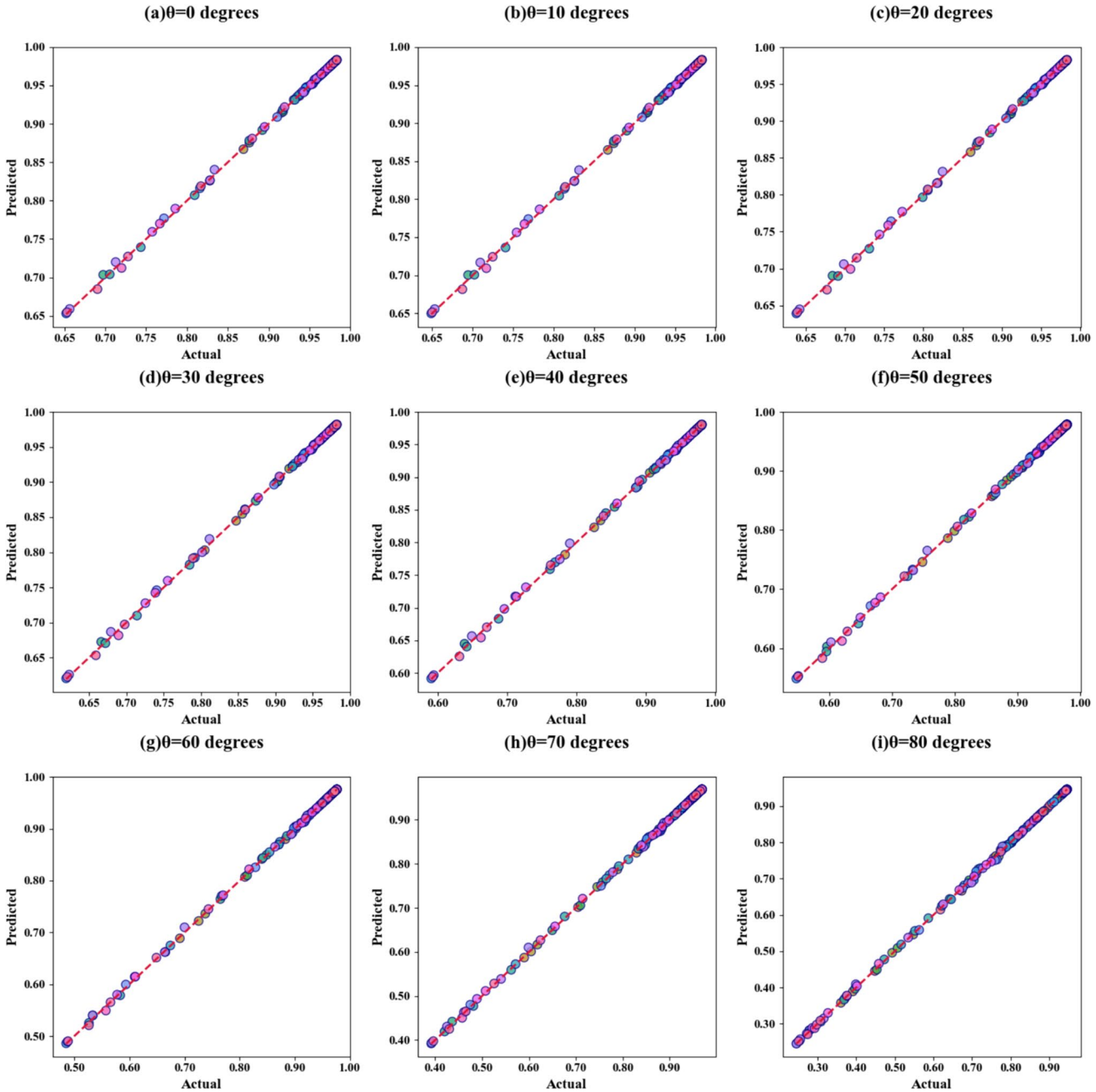

Fig. 14 Scatter plots for incident angle variation

incidence increases, consistent with Fresnel's equations and the principles of thin-film interference.

The color plot in Fig. 3 clearly demonstrates that as the angle of incidence increases, both the transmittance and the width of the transmission band also increase. This indicates that the sensor's response to incident angles broadens, enhancing its sensitivity and operational range.

In the third phase of parameter optimization, we conducted a systematic variation of the rectangular resonator width. This dimensional modification spanned from 1 to 4 µm, with incremental steps of 0.5 µm. The purpose of this parametric adjustment was to investigate its impact on transmittance across a broad spectral range of 0.1 to 1 THz. The outcomes of this width variation are presented in Fig. 4a, b of the simulation results.

The observed transmittance attenuations were quantified as follows: 12.46%, 13.17%, 14.10%, 15.53%, 18.43%, 34.44%, and 36.38%. These attenuation percentages

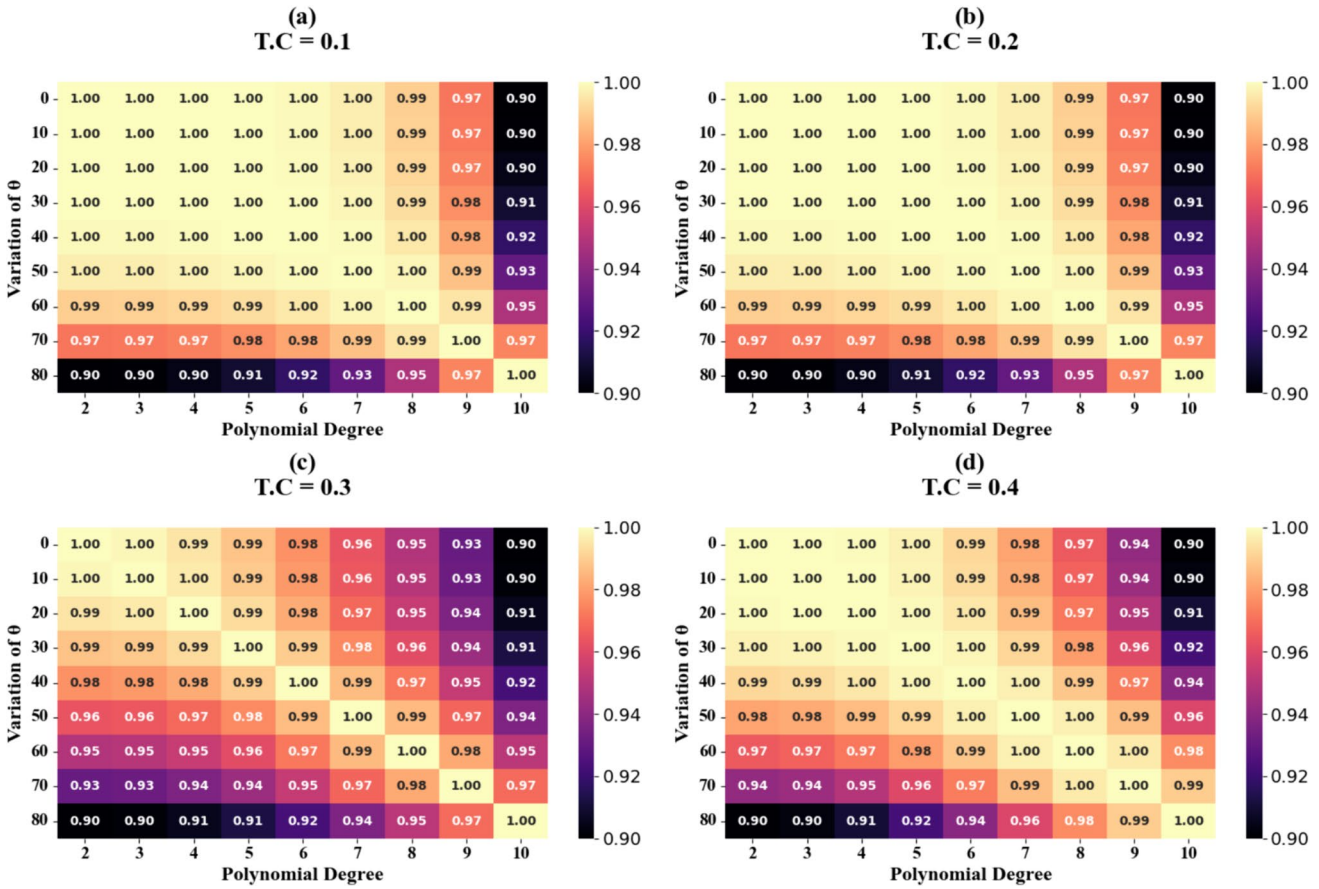

Fig. 15 Heat map plots for incident angle variation

correlate with specific resonator widths within the aforementioned dimensional range. Of particular note, as illustrated in Fig. 4b, the Fermi plot demonstrates a pronounced leftward shift in the transmittance response curve as a function of increasing rectangular resonator width. This spectral shift indicates an inverse relationship between resonator width and resonant frequency, with larger widths corresponding to lower frequency values.

In the fourth phase of parameter optimization, we systematically varied the height (h) of a rectangular resonator from 0.2 to 1.0 µm in increments of 0.2 µm. This investigation aimed to quantify the effect on transmittance across the frequency range of 0.1–0.3 THz. Figure 5a, b illustrates the results of these parametric variations. Significant transmittance reductions were observed, with values of 56.34%, 50.49%, 48.61%, 50.01%, and 53.31% corresponding to the respective resonator heights. Figure 5b presents these findings in a Fermi plot, demonstrating an inverse relationship between resonance frequency and resonator height. The data indicate a clear shift towards lower frequencies as h increases,

In the fifth phase of parameter optimization, we systematically varied the dimensions of the inner square resonator from 1.2 to 2.0 µm in 0.2-µm increments. This parametric study aimed to investigate the impact on transmittance characteristics across a frequency spectrum of 0.5–1.5 THz. Figure 6a, b illustrates the results of this parametric analysis, demonstrating significant reductions in transmittance percentages of 15.95%, 18.07%, 20.07%, 22.06%, and 24.46% across the 0.5–1.5-THz frequency range. Furthermore, Fig. 5b presents a complementary Fermi plot, visually depicting the inverse relationship between the height of the rectangular resonators and the resonant frequency during the simulation process.

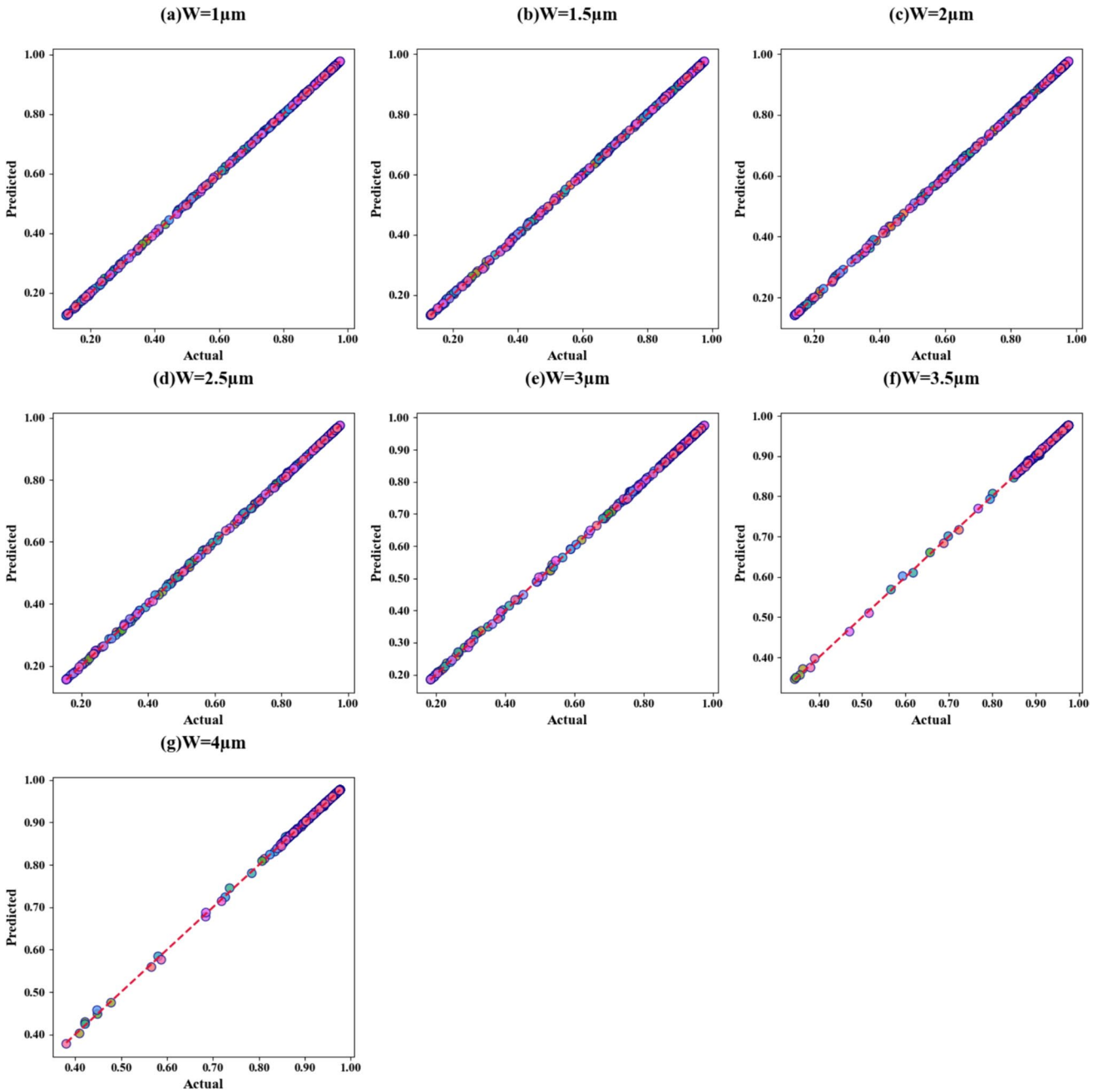

Fig. 16 Scatter plots for width of rectangular variation

In the final phase of parameter optimization, we systematically varied the dimensions of the outer square resonator from 6.5 to 9 µm in 0.5-µm increments. This modification was implemented to investigate the impact on transmittance across the frequency range of 0.5 to 1 THz. Figure 7a, b illustrates the resultant effects of these alterations, demonstrating transmittance reductions of 27.72%, 24.46%, 22.01%, 19.64%, 17.85%, and 16.59% at distinct frequencies within the specified range. Figure 5b presents a Fermi plot depicting the correlation between resonator size and transmittance. The plot indicates that as the outer square resonator dimensions increase from 6.5 to 9 µm, there is a corresponding expansion of the transmittance band, suggesting an enhanced range of frequencies at which efficient transmission through the resonator occurs

Following the successful optimization of the metasurface-based terahertz refractive index sensor structure, we proceeded to evaluate its efficacy in detecting hemoglobin concentrations. The established correlation between hemoglobin concentration and refractive index, as documented

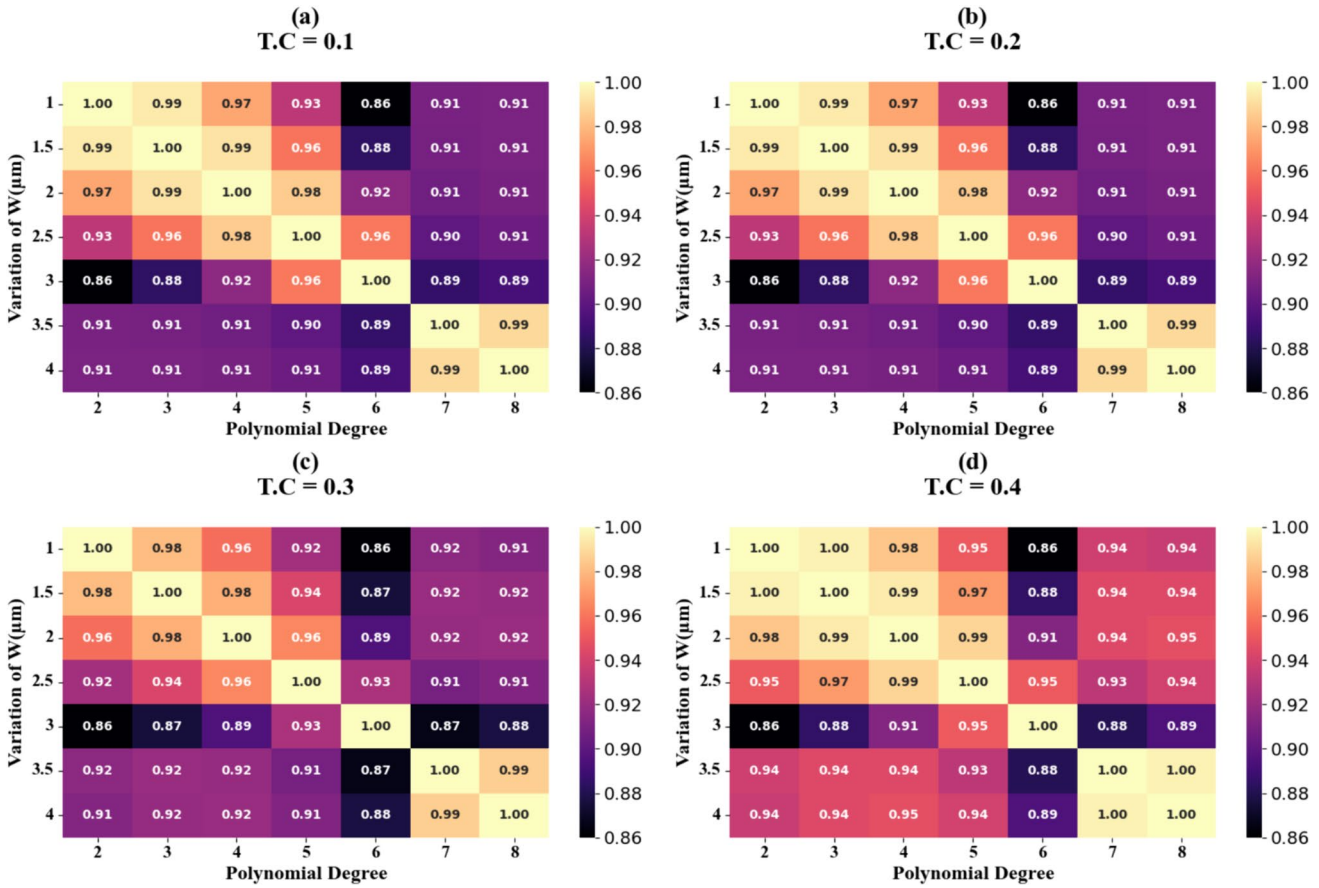

Fig. 17 Heat map plots for rectangular width variation

by [56]. To rigorously examine the sensor's performance, we conducted a series of simulations employing hemoglobin samples with concentrations ranging from 10 to 40 g/L. The concentration was incrementally increased by 10 g/L, yielding four discrete test points: 10 g/L, 20 g/L, 30 g/L, and 40 g/L. These concentrations correspond to refractive indices of 1.34, 1.36, 1.39, and 1.43, respectively, as determined by prior calibration. The relationship between hemoglobin concentration and transmittance response is fundamental to characterizing the sensor's performance. We have systematically demonstrated this relationship in Fig. 8, which illustrates the transmittance characteristics of the sensor design. Analysis of these results are used to evaluate key performance metrics, including the sensor's linearity, sensitivity, and overall efficacy in differentiating between varying hemoglobin concentrations within the clinically relevant range. This assessment provides crucial insights into the sensor's potential for practical implementation in hematological diagnostics and research.

Figure 8 in the study presents quantitative data illustrating the relationship between hemoglobin concentration and transmittance. The results demonstrate that as hemoglobin concentration increases, there is a corresponding decrease in transmittance, with each concentration level exhibiting a characteristic frequency at which the transmittance minimum is most pronounced.

For the sample with the lowest hemoglobin concentration, the maximum transmittance reduction of 10.72% was observed at 0.66 THz. As the concentration increased to the subsequent level, the peak reduction shifted to 10.65% at 0.64 THz. The third concentration level exhibited a 10.54% transmittance reduction at 0.635 THz. At the highest hemoglobin concentration tested, the sensor recorded a 10.41% transmittance reduction at 0.63 THz. This pattern demonstrates a consistent shift in the frequency of maximum transmittance reduction as a function of hemoglobin concentration. The subtle variations in both the transmittance reduction percentages and the corresponding frequencies provide critical data for sensor calibration and the determination of its sensitivity to incremental changes in hemoglobin concentration.

Furthermore, a comprehensive analysis was conducted to examine the correlation between resonance frequency with RIs and concentration. The results of this analysis are visually presented in Fig. 9a, b, respectively. The findings

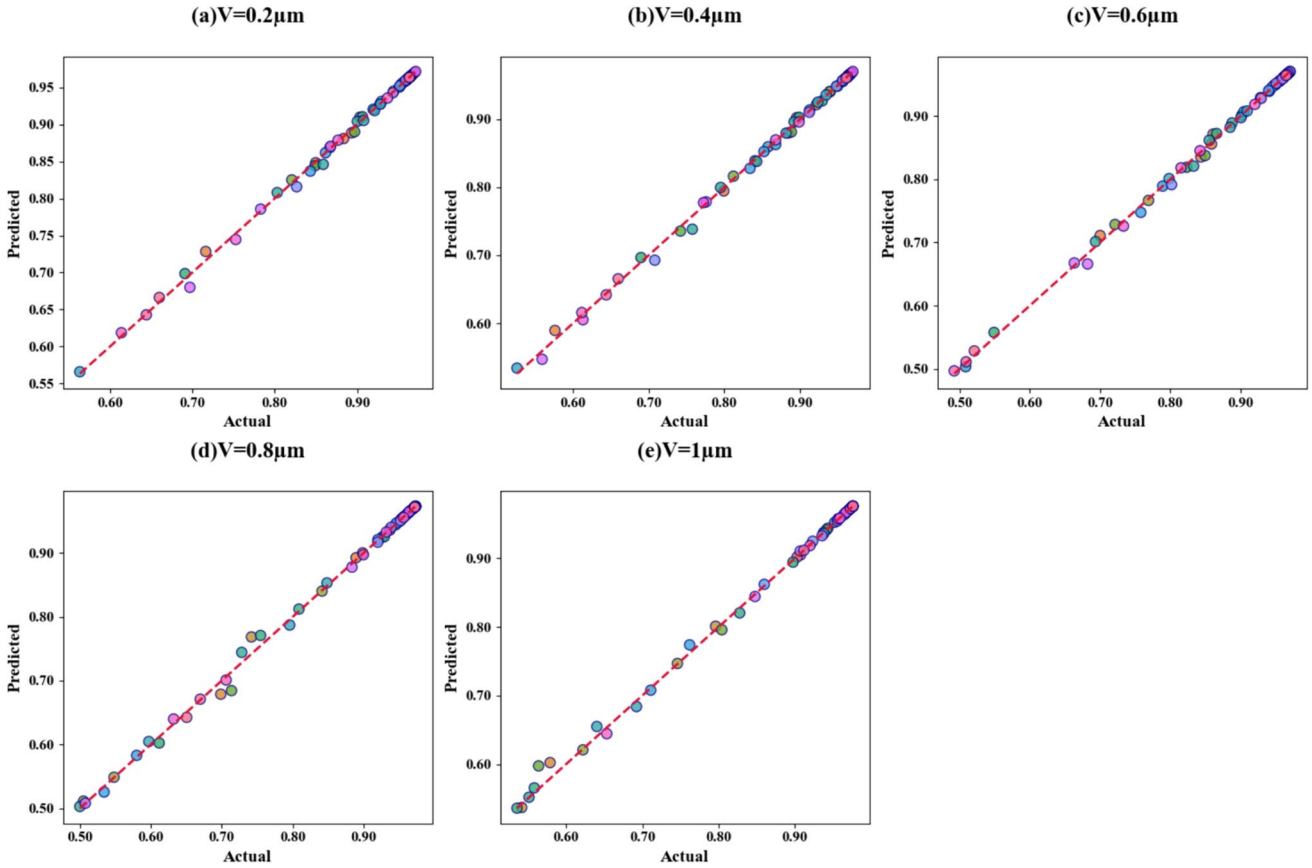

Fig. 18 Scatter plots for height of rectangular variation

demonstrate a strong positive correlation between these parameters.

The relationship between the refractive index (n) and the resonance frequency (F) is mathematically expressed through two linear equations:

$$F = -0.2935n + 1.0463 \tag{28}$$

$$F = -0.0009n + 0.6650 \tag{29}$$

The negative slopes in both equations (−0.2935 and −0.0009) indicate an inverse relationship between the variables. This means that as the refractive index increases. The high correlation coefficients (R^2 scores) of 0.9123 and 0.96988 were observed for these relationships. These R^2 values, being close to 1, indicate that the linear models provide an excellent fit to the experimental data, explaining 91.23% and 96.988% of the variance in the resonance frequency based on the refractive indices as well as concentration respectively. The difference in the magnitude of the slopes between Eqs. 28 and 29 is clearly demonstrated.

The electric field distribution results for the proposed sensor design are presented in Fig. 10a–f, illustrating the sensor's electromagnetic response at three critical frequencies: 0.4 THz, 0.65 THz, and 1 THz. At 0.65 THz, a notable anomaly is observed, characterized by a significant enhancement in absorption and a corresponding decrease in transmittance. This phenomenon is evident in Fig. 10c, d, where high-intensity electric field concentrations are visualized, indicative of increased electromagnetic energy absorption at this specific frequency. Conversely, the sensor's response at 0.4 THz and 1 THz demonstrates markedly different characteristics. As illustrated in Fig. 10a, b, e, f, these frequencies exhibit substantially lower electric field intensities. This distinct behavior suggests that at these frequencies, the sensor structure facilitates enhanced electromagnetic wave propagation, resulting in reduced absorption and consequently elevated transmittance levels. These observations highlight the frequency-dependent nature of the sensor's electromagnetic properties.

Table 2 provides a comprehensive analysis of the sensor's performance metrics across a range of frequencies (0.63–0.66 THz) and refractive indices (1.34–1.43 RIU) of blood components. The evaluated parameters include sensitivity and full width at half maximum (FWHM) among others. The sensor exhibits sensitivity values ranging from

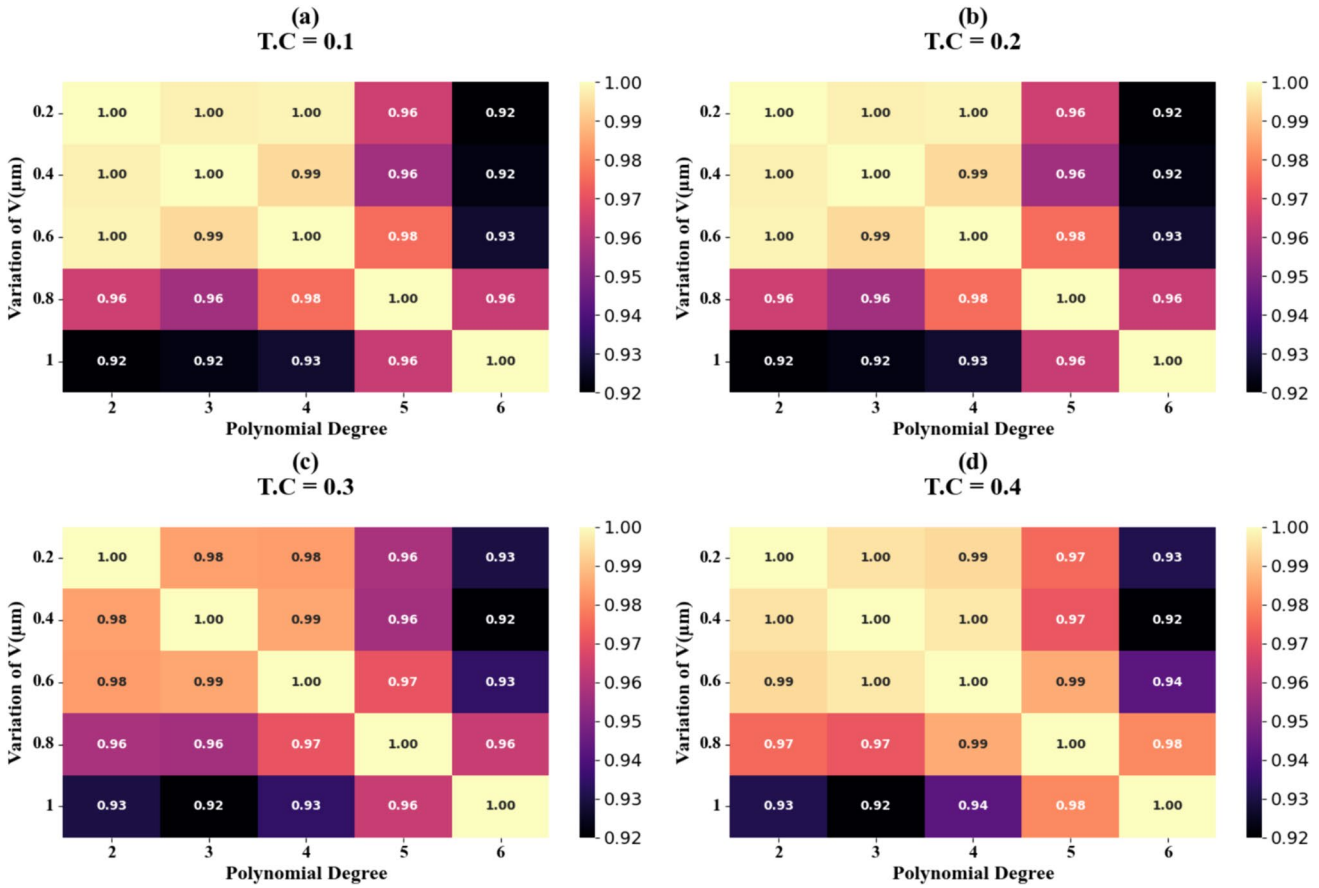

Fig. 19 Heat map plots for rectangular height variation

125 to 1000 GHzRIU^{-1}, demonstrating variable responsiveness to refractive index changes. The FWHM remains constant at 0.304 THz across the frequency spectrum, indicating a consistent spectral response. The FOM, calculated as the ratio of sensitivity to FWHM, spans from 0.411 to 3.289 RIU^{-1}. Q factors, ranging from 2.089 to 2.171, characterize the resonance peaks' sharpness and efficiency. Detection limits vary between 0.400 and 4.527 RIU, representing the minimum detectable refractive index change. The dynamic range, approximately 1.143 to 1.197, defines the span of measurable refractive indices. Sensor resolution values of 0.400 and 0.566 indicate the smallest discernible refractive index change. SNRs of 0.066 and 0.016 quantify the signal strength relative to background noise. Uncertainty values of 0.009 and 0.003 represent measurement variability, while the consistent detection accuracy of 3.289 underscores the sensor's precision in detecting refractive index changes.

We conducted a comparative analysis of the proposed sensor design with other cases. The evaluation focused on key performance metrics including operational range, sensitivity, and potential applications. A comprehensive overview of this comparison is presented in Table 3. The assessment showcases that the proposed sensor design demonstrates exceptional performance across all various parameters.

Figure 11a–d illustrates the encoding outcomes of the sensor design, demonstrating its application to binary encoding tasks through the adjustment of two chemical potentials, μc_1 and μc_2. The results demonstrate distinct patterns of transmittance based on different combinations of these chemical potentials. When both μc_1 and μc_2 are set to 0.1 eV, as shown in Fig. 11a, the sensor exhibits minimum transmittance drops. A similar outcome is observed in Fig. 11b, where μc_1 is maintained at 0.1 eV while μc_2 is increased to 0.9 eV. These configurations result in states of low transmittance, which can be interpreted as one set of binary values in the encoding scheme. In contrast, Fig. 11c, d depicts scenarios where close to perfect transmittance is achieved. This occurs when both μc_1 and μc_2 are set to 0.9 eV, as well as when μc_1 is 0.9 eV and $\mu c2$ is 0.1 eV. These high transmittance states represent the opposite binary values in the encoding system. The clear distinction between low and high transmittance states, achieved through various combinations of chemical potentials, demonstrates the sensor's capability for 2-bit encoding. By manipulating μc_1 and μc_2, the sensor

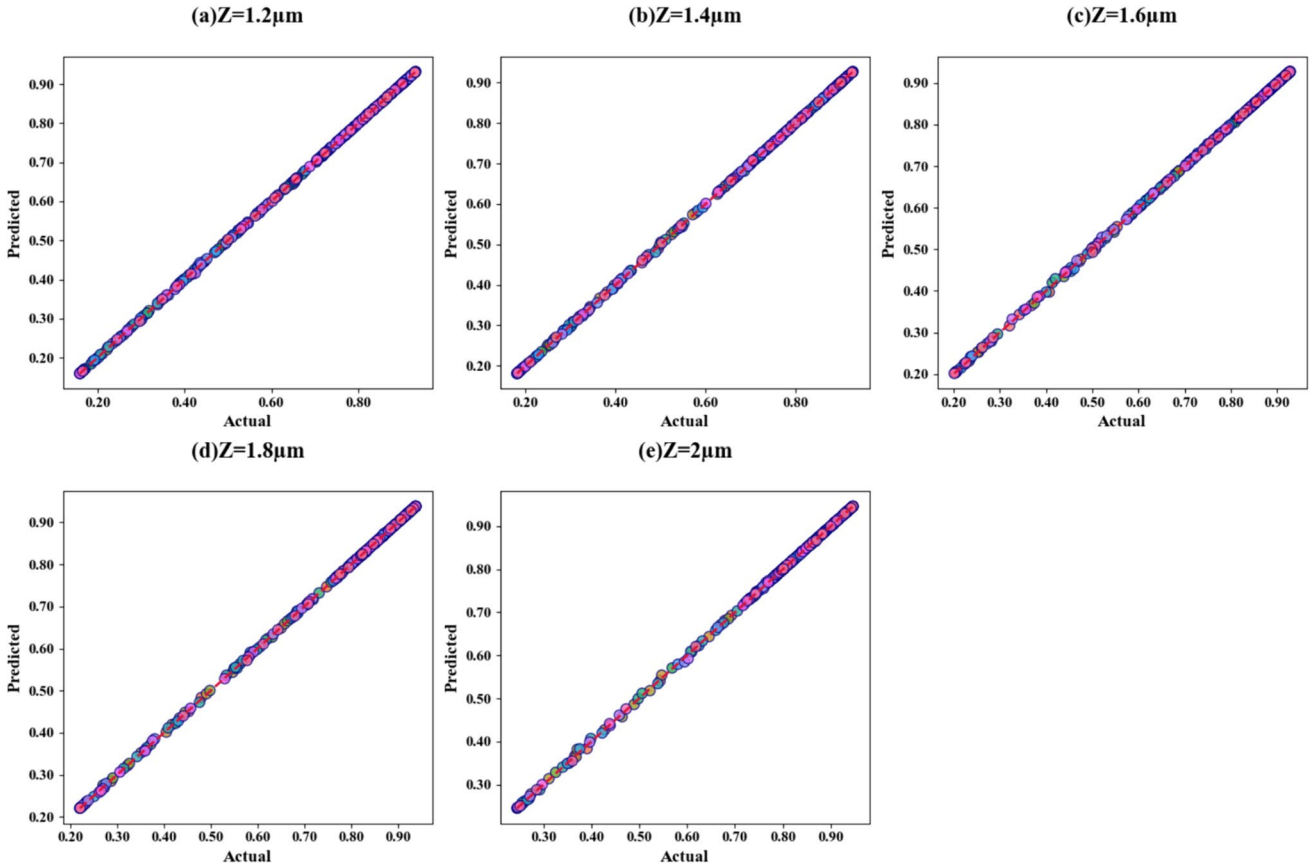

Fig. 20 Scatter plots for inner square resonator variation

can effectively switch between these states, offering a new approach to information encoding in sensor applications. This feature highlights the versatility and potential of the proposed sensor design in binary encoding tasks.

Machine Learning Optimization with Decision Tree Regressor

Decision tree regressor is a popular machine learning model used for both classification and regression tasks [60]. It is a tree-like structure that makes decisions based on asking a series of questions about the input features [61]. Decision trees consist of nodes, branches, and leaves. The topmost node is called the root node, internal nodes represent decision points, branches represent the possible answers to these decisions, and leaf nodes represent the final outcomes or predictions [62]. The tree makes decisions by traversing from the root node to a leaf node, following the appropriate branches based on the input features. At each internal node, a question is asked about a specific feature, and the path is chosen based on the answer. The training process of a decision tree involves recursively splitting the data based on the most informative features. The goal is to create pure or homogeneous subsets of data at each leaf node [63]. Common splitting criteria include Gini impurity, information gain, and variance reduction. The tree grows by selecting the best feature and split point at each node that maximizes the chosen splitting criterion. This process continues until a stopping condition is met, such as reaching a maximum depth or having a minimum number of samples in a leaf node [64]. Decision trees offer several advantages. Firstly, they are highly interpretable and visually intuitive, making them ideal for conveying decisions to non-technical audiences. Secondly, they can handle both numerical and categorical data effectively, minimizing the need for extensive data preprocessing. Thirdly, decision trees are non-parametric, meaning they can capture complex, non-linear relationships in the data without making assumptions about the underlying data distribution. Lastly, decision trees provide a straightforward way to assess feature importance, aiding in feature selection and understanding the key predictors influencing outcomes. Despite their advantages, decision trees also have several limitations. Firstly, they are susceptible to overfitting, particularly when they are allowed to grow excessively deep, which can result in poor performance when applied to new, unseen data. Secondly, decision trees can exhibit instability, meaning small variations in the training data

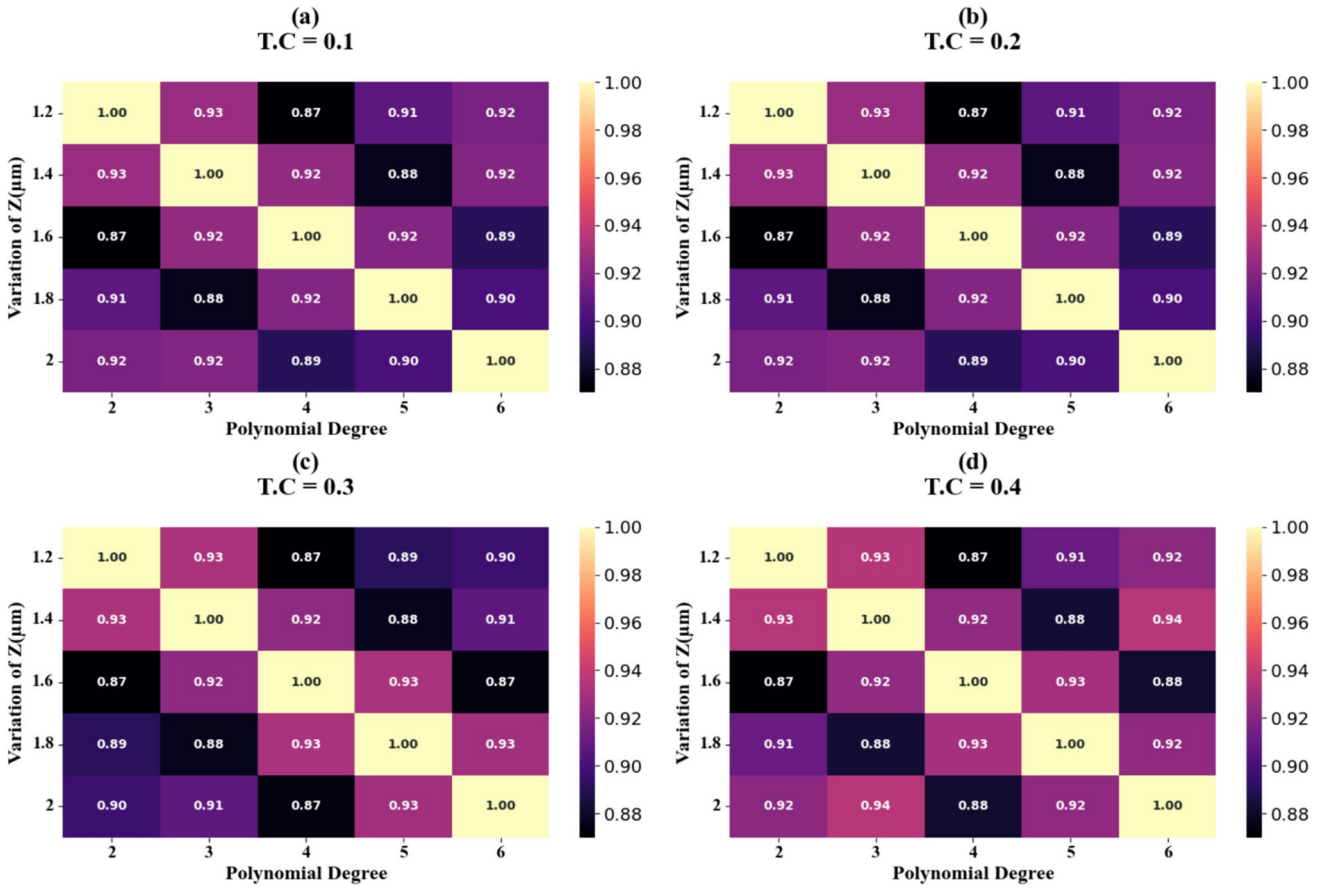

Fig. 21 Heat map plots for inner square resonator variation

could lead to significantly different tree structures, impacting the model's reliability. Thirdly, in datasets where classes are imbalanced, decision trees may show a bias towards the dominant class, potentially leading to less accurate predictions for minority classes. Important hyperparameters for decision trees include maximum depth, minimum samples per leaf, minimum samples for split, and maximum number of features. These parameters can be tuned using techniques like cross-validation to optimize model performance.

Mathematical Equations for the Model Analysis

Mean Squared Error (MSE)

Mean squared error is used for evaluating splits and measuring the quality of predictions:

$$\mathrm{MSE} = \left(\frac{1}{n}\right) \times \Sigma\left(y_i - \hat{y}_i\right)^2 \tag{30}$$

where n is the number of samples, y_i is the actual value, and $\hat{y}_i$ is the predicted value.

Mean Absolute Error (MAE)

Mean absolute error is an alternative to MSE, less sensitive to outliers:

$$\mathrm{MAE} = \left(\frac{1}{n}\right) \times \Sigma\left|y_i - \hat{y}_i\right| \tag{31}$$

Variance reduction is used to evaluate the quality of a split:

$$\mathrm{A} = U - \frac{K}{N} \times \mathrm{W} - \frac{P}{N} \times \mathrm{B} \tag{32}$$

where A is the variance reduction, U is the variance of the parent node, K and P are the number of samples in left and right child nodes, N is the total number of samples in the parent node, and W and B are the variances of the left and right child nodes.

Leaf Node Prediction

The prediction at a leaf node is typically the mean of the target values in that node:

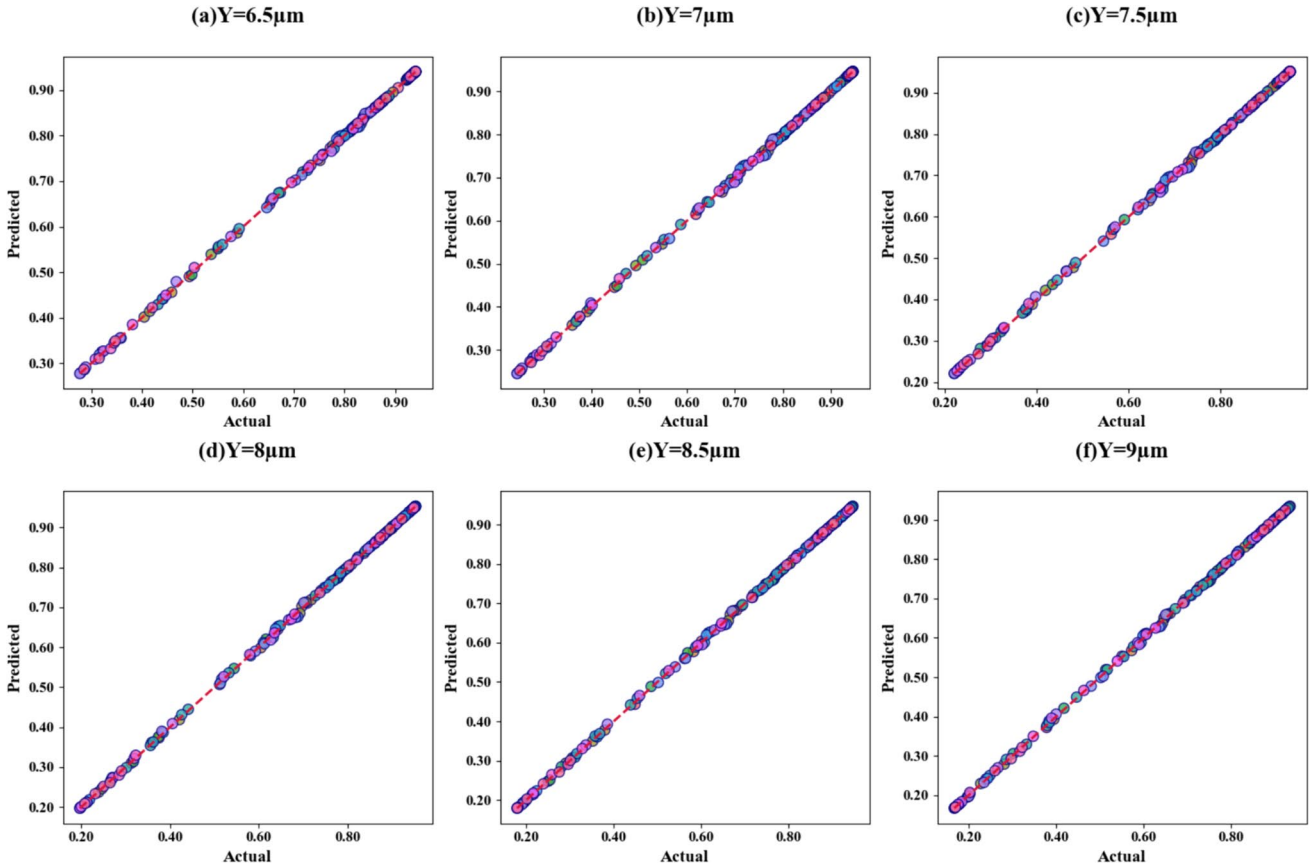

Fig. 22 Scatter plots for outer square resonator variation

$$\hat{y} = \frac{1}{q} \times \Sigma y_i \tag{33}$$

Pruning Cost Function

Pruning cost function is used in post-pruning to balance complexity and accuracy:

$$\hat{y} = \frac{1}{q} \times \Sigma y_i \tag{34}$$

$$\text{Cost}(T) = \Sigma(\text{leaf nodes})[\text{MSE(leaf)}] + \alpha|T| \tag{35}$$

where T is the tree, $|T|$ is the number of leaf nodes, and α is the complexity parameter.

R-Squared (Coefficient of Determination)

R-squared is used to evaluate the overall performance of the regressor:

$$R^2 = 1 - (\text{SSR}/\text{SST}) \tag{36}$$

where SSR is the sum of squared residuals, SST is the total sum of squares, and $\bar{y}$ is the mean of observed values.

In these experiments, the frequency of simulation is treated as the dependent variable, and a decision tree regressor is essentially chosen for its ability to predict absorption values accurately. The performance of the prediction models is evaluated using the R^2 score, which measures how well the predicted values align with the actual observations.

The performance of the models, trained using various combinations of graphene potential and polynomial degree parameters, is represented in Fig. 12a–i through scatter plots and in Fig. 13a–d via heat maps. These graphical representations demonstrate the influence of diverse input configurations on the models' overall efficacy. Analysis of the scatter plots depicts that an optimal coefficient of determination (R^2) of 1 is achieved for test case (TC) values ranging from 0.1 to 0.3 across all graphene potential combinations (GCP) examined.

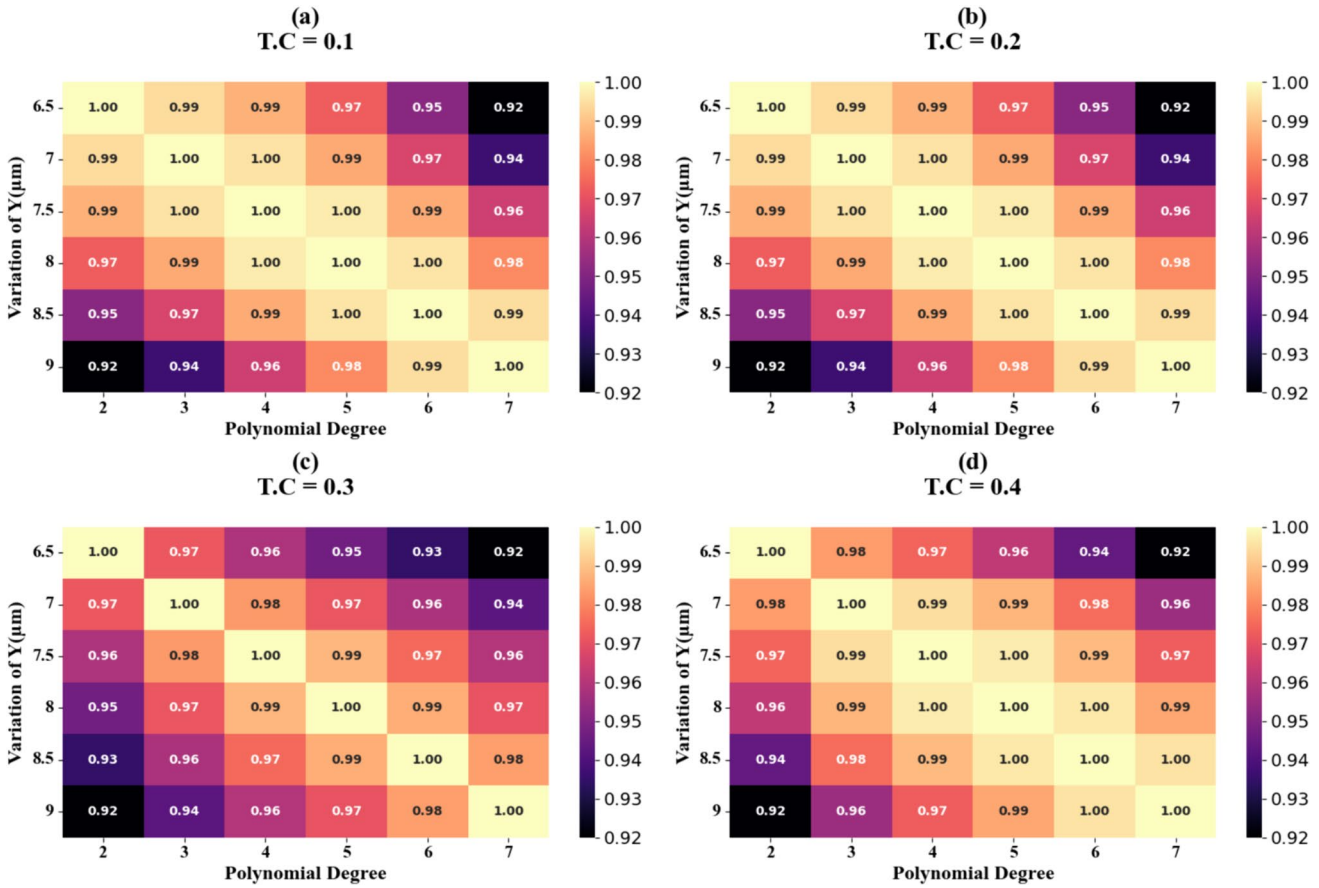

Fig. 23 Heat map plots for outer square resonator variation

The heat maps demonstrate a correlation between increasing polynomial degree and R^2 scores. For TC values of 0.1 and 0.2, the R^2 scores span from 0.89 to 1, whereas for TC values of 0.3 and 0.4, the R^2 scores range from 0.9 to 1. This trend suggests that higher polynomial degrees generally yield improved model performance, particularly for larger TC values.

The effectiveness of the models, which were trained using different combinations of incidence angles and polynomial degree parameters, is illustrated in two ways: through scatter plots in Fig. 14a–i and heat maps in Fig. 15a–d. These representations showcase how various input configurations affect the models' overall performance. Examination of the scatter plots exemplifies that the models achieve a perfect coefficient of determination (R^2) of 1 for test case (TC) values between 0.15 and 0.45, consistent across all cases studied. The heat maps demonstrate a trend where higher polynomial degrees correspond to improved R^2 scores. For TC values ranging from 0.1 to 0.4, the R^2 scores fall between 0.90 and 1.

The models' performance, trained on varying combinations of rectangular widths and polynomial degree parameters, is rigorously evaluated using scatter plots depicted in Fig. 16a–g and heat maps in Fig. 17a–d. These graphical analyses provide illustration into the influence of different input configurations on the models' predictive accuracy. The scatter plots consistently demonstrate an optimal coefficient of determination (R^2) of 1 for test case (TC) values within the range of 0.25 to 0.35 across all cases investigated. The heat maps further showcase a positive correlation between increased polynomial degrees and enhanced R^2 values. Particularly, for TC values between 0.1 and 0.3, the R^2 values range from 0.91 to 1, while for TC = 0.4, the R^2 values are observed to fall between 0.94 and 1.

The performance of the models, trained on various combinations of rectangular heights and polynomial degree parameters, is thoroughly assessed using scatter plots shown in Fig. 18a–e and heat maps in Fig. 19a–d. These representations highlight the impact of different input configurations on the models' predictive accuracy. The scatter plots consistently showcase an optimal coefficient of determination (R^2) of 1 for test case (TC) values ranging from 0.15 to 0.45 across all scenarios studied. The heat maps further illustrate a positive correlation between higher polynomial degrees and improved R^2 values. Essentially, for TC values between 0.1 and 0.2, R^2 values range from 0.92 to 1, while for TC = 0.3 and 0.4, R^2 values are observed between 0.93 and 1.

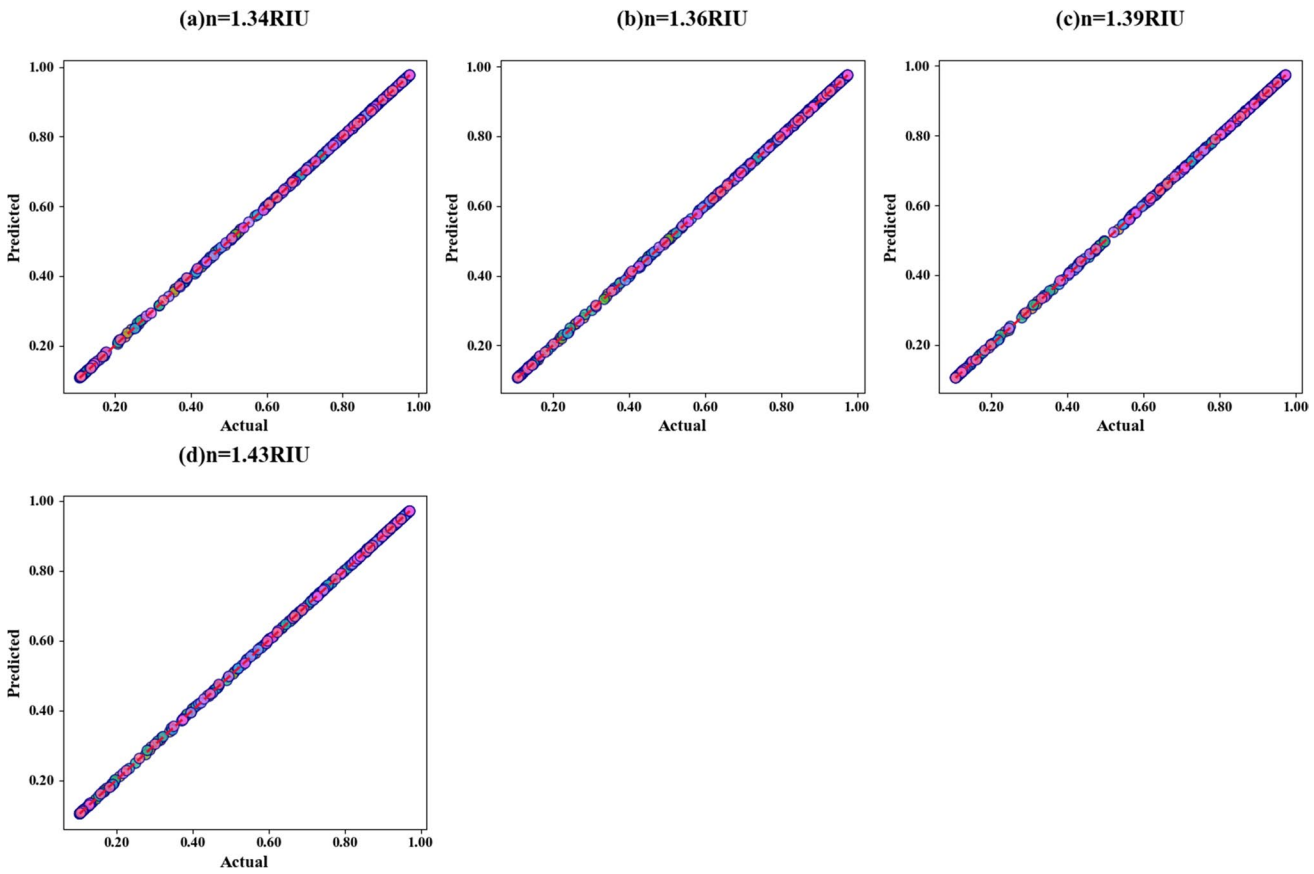

Fig. 24 Scatter plots for the variation of RIs for detection analysis

The performance of the models, trained on diverse combinations of inner square resonator dimensions and polynomial degree parameters, is systematically evaluated using scatter plots (Fig. 20a–e) and heat maps (Fig. 21a–d). These graphical representations depict the influence of varying input configurations on the models' predictive accuracy. The scatter plots consistently demonstrate an optimal coefficient of determination (R^2) of 1 for test case (TC) values ranging from 0.35 to 0.45 across all examined scenarios. Moreover, the heat maps demonstrate a positive correlation between increased polynomial degrees and enhanced R^2 values. Notably, for TC values of 0.1, 0.2, and 0.4, the R^2 values span from 0.92 to 1, while for TC = 0.3, the R^2 values are observed within the range of 0.90 to 1.

The models' performance, trained on diverse combinations of outer square resonator dimensions and polynomial degree parameters, is rigorously evaluated through scatter plots (Fig. 22a–f) and heat maps (Fig. 23a–d). These graphical analyses exemplify the effects of varying input configurations on the models' predictive accuracy. The scatter plots consistently demonstrate an optimal coefficient of determination (R^2) of 1 for test case (TC) values in the range of 0.25 to 0.55 across all scenarios studied. Furthermore, the heat maps exhibit a clear positive correlation between increasing polynomial degrees and enhanced R^2 values. Notably, for TC values of 0.1, 0.2, 0.3, and 0.4, the R^2 values are observed to span from 0.92 to 1, indicating high predictive accuracy.

The effectiveness of the models, which were trained using various combinations of refractive indices and polynomial degree settings, is thoroughly assessed using visual representations. Scatter plots (shown in Fig. 24a–d) and heat maps (illustrated in Fig. 25a–d) are employed to demonstrate how different input configurations impact the models' predictive accuracy. Across all examined cases, the scatter plots consistently show an ideal coefficient of determination (R^2) of 1 for test case (TC) values ranging from 0.5 to 0.15. The heat maps depicts that as polynomial degrees increase, so do the R^2 values, indicating improved accuracy. For TC values of 0.1, 0.2, 0.3, and 0.4, the models achieve high predictive accuracy, with R^2 values ranging from 0.95 to 1. This suggests strong performance across various test conditions.

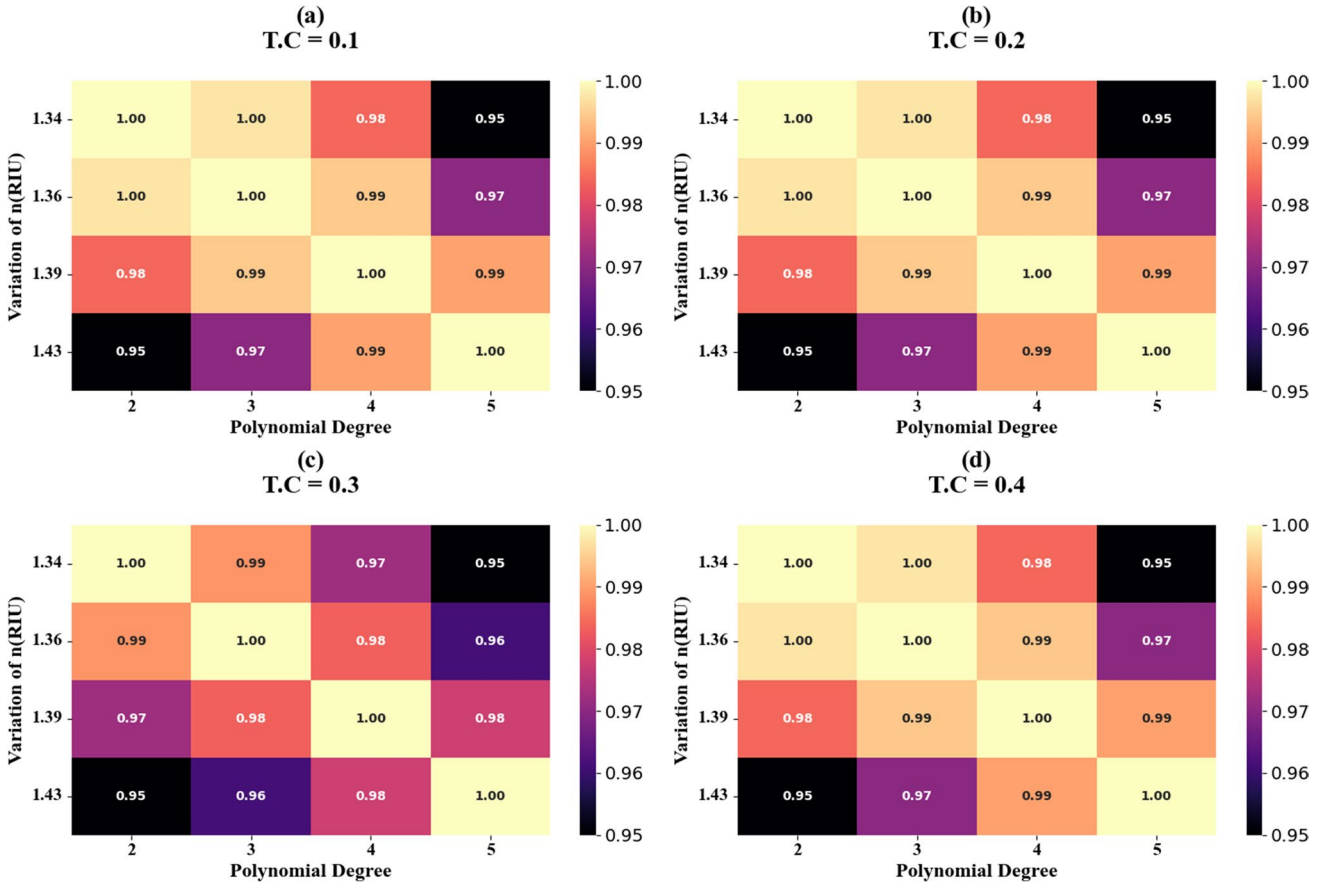

Fig. 25 Heat map plots for the variation of RIs for detection analysis

Conclusion

In summary, this study has presented a terahertz-based biosensor for hemoglobin detection. The optimized sensor structure, featuring a hierarchical resonator arrangement, demonstrates remarkable sensitivity of up to 1000 GHzRIU^{-1} and a figure of merit of 3.289 RIU^{-1}. The sensor's ability to detect hemoglobin concentrations ranging from 10 to 40 g/L with high accuracy showcases its potential for real-world medical diagnostic applications, particularly in point-of-care settings where rapid and precise hemoglobin quantification is crucial. The analysis of electric field distributions demonstrates a frequency-dependent absorption behavior, with peak absorption observed at 0.65 THz. Furthermore, the implementation of machine learning optimization using a decision tree regressor exemplifies perfect prediction accuracy across various parameter combinations. This successful integration of artificial intelligence techniques with biosensor design represents a significant step towards developing more intelligent and adaptive sensing systems. While the results are highly promising, future work should focus on experimental validation of the simulated performance, investigation of the sensor's behavior with complex biological samples, and exploration of its potential in detecting other biomolecules. Additionally, further research into miniaturization and integration with existing medical devices could accelerate the sensor's transition from laboratory concept to practical application.

Acknowledgements The authors thank the National Forensic Sciences University for allowing them to use the digital computer laboratory for this research.

Author Contribution Conceptualization: JW; methodology: CL, AO, NM, CW, and WL; software: JW; validation: all authors; writing—original draft preparation: all authors; formal analysis: CL, AO, NM, CW, and WL; writing—review and editing: all authors. All authors have read and agreed to the published version of the manuscript.

Data Availability The data supporting the findings in this work are available from the corresponding author with a reasonable request.

Declarations

Ethical Approval Not applicable.

Competing Interests (not applicable)

References

1. Haleem A, Javaid M, Singh RP, Suman R, Rab S (2021) Biosensors applications in medical field: a brief review. Sensors International 2. https://doi.org/10.1016/j.sintl.2021.100100
2. Singh AK, Mittal S, Das M, Saharia A, Tiwari M (2023) Optical biosensors: a decade in review. Alexandria Engineering Journal 67:673–691. https://doi.org/10.1016/j.aej.2022.12.040
3. Pillai S, Upadhyay A, Sayson D, Nguyen BH, Tran SD (2022) Advances in medical wearable biosensors: design, fabrication and materials strategies in healthcare monitoring. Molecules 27(1). https://doi.org/10.3390/molecules27010165
4. Wu J, Liu H, Chen W, Ma B, Ju H (2023) Device integration of electrochemical biosensors. Nat. Rev. Bioeng. 1(5):346–360. https://doi.org/10.1038/s44222-023-00032-w
5. Hayat K (2024) Biosensors precision in healthcare: a Scientific Odyssey. Pakistan Biomed. J.:1. https://doi.org/10.54393/pbmj.v7i01.1026
6. J. Swain, S. Swain, D. Singh, A. Jena, R. Samantaray, and R. Sahu, "Role of piezoelectric biosensors," in Point-of-Care Biosensors for Infectious Diseases, 2023, pp. 129–145. doi: https://doi.org/10.1002/9783527837946.ch7.
7. Mehrotra P (2016) Biosensors and their applications - a review. Journal of Oral Biology and Craniofacial Research 6(2):153–159. https://doi.org/10.1016/j.jobcr.2015.12.002
8. Shan CW, Chen Z, Han GC, Feng XZ, Kraatz HB (2024) Electrochemical immuno-biosensors for the detection of the tumor marker alpha-fetoprotein: a review. Talanta 271. https://doi.org/10.1016/j.talanta.2024.125638
9. Musa AM, Kiely J, Luxton R, Honeychurch KC (2023) An electrochemical screen-printed sensor based on gold-nanoparticle-decorated reduced graphene oxide–carbon nanotubes composites for the determination of 17-β estradiol. Biosensors 13(4). https://doi.org/10.3390/bios13040491
10. Rasheed S, Kanwal T, Ahmad N, Fatima B, Najam-ul-Haq M, Hussain D (2024) Advances and challenges in portable optical biosensors for onsite detection and point-of-care diagnostics. TrAC - Trends in Analytical Chemistry 173. https://doi.org/10.1016/j.trac.2024.117640
11. Li S et al (2023) Electrochemical biosensors for whole blood analysis: recent progress, challenges, and future perspectives. Chemical Reviews 123(12):7953–8039. https://doi.org/10.1021/acs.chemrev.1c00759
12. Ji G, Tian J, Xing F, Feng Y (2022) Optical biosensor based on graphene and its derivatives for detecting biomolecules. International Journal of Molecular Sciences 23(18). https://doi.org/10.3390/ijms231810838
13. Yazdanpanah S, Rabiee M, Tahriri M, Abdolrahim M, Tayebi L (2015) Glycated hemoglobin-detection methods based on electrochemical biosensors. TrAC - Trends in Analytical Chemistry 72:53–67. https://doi.org/10.1016/j.trac.2015.03.019
14. Wu H, Wang X, Qiao M, Zhang H, Jin X, Fan S (2015) Enhancing sensitivity of hemoglobin-based electrochemical biosensor by using protein conformational intermediate. Sensors Actuators, B Chem. 221:694–699. https://doi.org/10.1016/j.snb.2015.07.025
15. Rahimzadegan A et al (2022) A comprehensive multipolar theory for periodic metasurfaces. Adv. Opt. Mater. 10(10). https://doi.org/10.1002/adom.202102059
16. Wekalao J, Mandela N, Obed A, Bouhenna A (2024) Design and evaluation of tunable terahertz metasurface biosensor for malaria detection with machine learning optimization using artificial intelligence. Plasmonics (123456789). https://doi.org/10.1007/s11468-024-02491-2
17. Saifullah Y, He Y, Boag A, Yang GM, Xu F (2022) Recent progress in reconfigurable and intelligent metasurfaces: a comprehensive review of tuning mechanisms, hardware designs, and applications. Advanced Science 9(33). https://doi.org/10.1002/advs.202203747
18. Chang S, Guo X, Ni X (2018) Optical metasurfaces: progress and applications. Annual Review of Materials Research 48:279–302. https://doi.org/10.1146/annurev-matsci-070616-124220
19. Wekalao J, Patel SK, Ben Khalifa S, Chebaane S, Armghan A, Saidani T (2024) Optical-based aqueous solution detection by graphene metasurface surface plasmon resonance biosensor with behavior prediction using polynomial regression. Plasmonics. https://doi.org/10.1007/s11468-024-02464-5
20. So S, Mun J, Park J, Rho J (2023) Revisiting the design strategies for metasurfaces: fundamental physics, optimization, and beyond. Advanced Materials 35(43). https://doi.org/10.1002/adma.202206399
21. Ding F, Yang Y, Deshpande RA, Bozhevolnyi SI (2018) A review of gap-surface plasmon metasurfaces: fundamentals and applications. Nanophotonics 7(6):1129–1156. https://doi.org/10.1515/nanoph-2017-0125
22. Leitis A et al (2020) All-dielectric programmable Huygens' metasurfaces. Adv. Funct. Mater. 30(19). https://doi.org/10.1002/adfm.201910259
23. J. Wekalao, S. K. Patel, and F. Ahmed, "Graphene metasurfaces - based surface plasmon resonance biosensor for virus detection with sensitivity enhancement using perovskite materials," no. 123456789, 2024.
24. Razaq A, Bibi F, Zheng X, Papadakis R, Jafri SHM, Li H (2022) Review on graphene-, graphene oxide-, reduced graphene oxide-based flexible composites: from fabrication to applications. Materials 15(3). https://doi.org/10.3390/ma15031012
25. J. Wekalao, G. P. Srinivasan, S. K. Patel, and F. A. Al-zahrani, "Optimization of graphene-based biosensor design for haemoglobin detection using the gradient boosting algorithm for behaviour prediction".
26. Tiwari SK, Sahoo S, Wang N, Huczko A (2020) Graphene research and their outputs: status and prospect. Journal of Science: Advanced Materials and Devices 5(1):10–29. https://doi.org/10.1016/j.jsamd.2020.01.006
27. Anushkannan NK, Wekalao J, Patel SK, Al-Zahrani FA (2024) Design of encoded and tunable graphene-gold metasurface-based surface plasmon resonance sensors for glucose detection in the terahertz regime. Plasmonics (123456789). https://doi.org/10.1007/s11468-024-02452-9
28. Jiříčková A, Jankovský O, Sofer Z, Sedmidubský D (2022) Synthesis and applications of graphene oxide. Materials 15(3). https://doi.org/10.3390/ma15030920
29. Yildiz G, Bolton-Warberg M, Awaja F (2021) Graphene and graphene oxide for bio-sensing: general properties and the effects of graphene ripples. Acta Biomaterialia 131:62–79. https://doi.org/10.1016/j.actbio.2021.06.047
30. Wekalao TTJ, Mandela N, Apochi O, Lefu C (2024) Nanoengineered graphene metasurface surface plasmon resonance sensor for precise hemoglobin detection with AI-assisted performance prediction. Plasmonics
31. Bhuyan MSA, Uddin MN, Islam MM, Bipasha FA, Hossain SS (2016) Synthesis of graphene. International Nano Letters 6(2):65–83. https://doi.org/10.1007/s40089-015-0176-1
32. Alsaif H et al (2024) Design and optimization of a MXene-based terahertz surface plasmon resonance sensor for malaria detection. Plasmonics (123456789). https://doi.org/10.1007/s11468-024-02455-6
33. Wekalao J, Mandela N, Muheki J, Zaid A (2024) Design and analysis of a terahertz metasurface - based refractive index sensor for hemoglobin detection with behaviour prediction using polynomial regression. Plasmonics (123456789). https://doi.org/10.1007/s11468-024-02445-8

34. Jacob NP, Ashokkumar W, Patel NSK (2024) Design and analysis of a plasmonic metasurface - based graphene sensor for highly sensitive and label - free detection of COVID - 19 biomarkers. Plasmonics (123456789). https://doi.org/10.1007/s11468-024-02442-x
35. Patel SK, Wekalao J, Mandela N, Al-Zahrani FA (2024) Design of encoded graphene-gold metasurface-based circular ring and square sensors for brain tumor detection and optimization using XGBoost algorithm. Diam. Relat. Mater. 148:111439. https://doi.org/10.1016/j.diamond.2024.111439
36. J. Wekalao, O. Alsalman, H. Patel, R. Manvani, and S. K. Patel, Swift detection of heavy metals in water by encoded graphene–gold-metasurface sensor, vol. 56, no. 7. Springer US, 2024. doi: https://doi.org/10.1007/s11082-024-07140-w.
37. Alsharari M, Wekalao J, Patel SK, Kumar A, Aliqab UK, Armghan A (2024) Enhanced sensing efficiency of ultra - narrow band graphene - based surface plasmon resonance refractive index sensor for biochemical applications and environmental monitoring. Plasmonics (123456789). https://doi.org/10.1007/s11468-024-02372-8
38. Aliqab K, Wekalao J, Alsharari M, Armghan A, Agravat D, Patel SK (2023) Designing a graphene metasurface organic material sensor for detection of organic compounds in wastewater. Biosensors 13(8). https://doi.org/10.3390/bios13080759
39. Almawgani AHM, Wekalao J, Patel SK, Alzahrani A, Gumaih HS, Armghan A (2024) Optimization of graphene-based square slotted surface plasmon resonance refractive index biosensor for accurate detection of pregnancy. Plasmonics (123456789). https://doi.org/10.1007/s11468-024-02290-9
40. Almawgani AHM, Wekalao J, Patel SK, Alzahrani A, Gumaih HS (2024) Design and development of a split ring resonator and circular disc metasurface based graphene / gold surface plasmon resonance sensor for illicit drugs detection. Plasmonics (123456789). https://doi.org/10.1007/s11468-024-02306-4
41. Wekalao J, Albargi HB, Patel SK, Jalalah M, Almawgani AHM (2024) Terahertz optical ultrasensitive glucose detection using graphene and silver surface plasmon resonance metasurfaces for biomedical applications. Plasmonics (123456789). https://doi.org/10.1007/s11468-024-02278-5
42. J. Muheki, J. Wekalao, H. B. Albargi, M. Jalalah, and A. H. M. Almawgani, "A graphene gold metasurface inspired surface plasmon resonance sensor designed for terahertz applications in sensing and detection of heavy metals in water," 2024.
43. Wekalao J, Alsalman O, Shobhit RM (2024) Graphene biosensor design based on glass substrate for forensic detection of illicit drugs. Opt. Quantum Electron. https://doi.org/10.1007/s11082-024-06690-3
44. Wekalao J, Kumar A, Albargi UHB, Jalalah M, Almawgani AHM (2024) Graphene and gold metasurface - based terahertz surface plasmon resonance sensor for explosive detection. Plasmonics (123456789). https://doi.org/10.1007/s11468-024-02229-0
45. Patel SK, Wekalao J, Albargi HB, Jalalah M, Almawgani AHM (2024) Design and simulation of metasurface - enhanced graphene biosensors for cancer biomarker detection. Plasmonics (123456789). https://doi.org/10.1007/s11468-024-02224-5
46. Wekalao J et al (2023) Graphene-based THz surface plasmon resonance biosensor for hemoglobin detection applicable in forensic science. Plasmonics. https://doi.org/10.1007/s11468-023-02146-8
47. Alsalman O, Wekalao J, Arun Kumar U, Agravat D, Parmar J, Patel SK (2023) Design of Split Ring Resonator Graphene Metasurface Sensor for Efficient Detection of Brain Tumor. Plasmonics (123456789). https://doi.org/10.1007/s11468-023-02002-9
48. Patel SK, Wekalao J, Alsalman O, Surve J, Parmar J, Taya SA (2023) Development of surface plasmon resonance sensor with enhanced sensitivity for low refractive index detection. Opt. Quantum Electron. 55(11). https://doi.org/10.1007/s11082-023-05265-y
49. Wekalao J, Patel SK, Alsalman O, Surve J, Anushkannan NK, Parmar J (2023) Waterborne Bacteria Detecting Highly Sensitive Graphene Metasurface Based Cost-Efficient and Efficient Refractive Index Sensors. Plasmonics (123456789). https://doi.org/10.1007/s11468-023-01983-x
50. Wekalao J, Alsalman O, Natraj NA, Surve J, Parmar J, Patel SK (2023) Design of Graphene Metasurface Sensor for Efficient Detection of COVID-19. Plasmonics (123456789). https://doi.org/10.1007/s11468-023-01946-2
51. Wekalao J, Patel SK, Anushkannan NK, Alsalman O, Surve J, Parmar J (2023) Design of ring and cross shaped graphene metasurface sensor for efficient detection of malaria and 2 bit encoding applications. Diam. Relat. Mater. 139:110401. https://doi.org/10.1016/j.diamond.2023.110401
52. Patel SK, Parmar J, Katkar V (2022) Ultra-broadband, wide-angle plus-shape slotted metamaterial solar absorber design with absorption forecasting using machine learning. Sci. Rep. 12(1):1–14. https://doi.org/10.1038/s41598-022-14509-y
53. Patel SK et al (2022) Graphene based highly sensitive refractive index sensor using double split ring resonator metasurface. Opt. Quantum Electron. 54(3). https://doi.org/10.1007/s11082-022-03600-3
54. Abbaszadeh A, Rash-Ahmadi S (2024) A surface plasmon resonance sensor based on photonic crystal fiber composed of magnesium fluoride and graphene layers to detect aqueous solutions. Opt. Quantum Electron. 56(6). https://doi.org/10.1007/s11082-024-06853-2
55. Płaneta S, Bartusik-Aebisher D, Aebisher D (2023) Hemoglobin. In: The Biochemical Guide to Proteins, pp 117–121. https://doi.org/10.5005/jp/books/13014_24
56. Patel SK, Surve J, Parmar J, Natesan A, Katkar V (2023) Graphene-Based Metasurface Refractive Index Biosensor for Hemoglobin Detection: Machine Learning Assisted Optimization. IEEE Trans. Nanobioscience 22(2):430–437. https://doi.org/10.1109/TNB.2022.3201237
57. J. Surve, R. Jadeja, T. Parmar, J. Parmar, and J. Parmar, "A Terahertz-Based Graphene Metasurface Sensor for Hemoglobin Detection with High Q Factor and Low Figure of Merit," in Terahertz Devices, Circuits and Systems: Materials, Methods and Applications, 2022, pp. 41–51. doi: https://doi.org/10.1007/978-981-19-4105-4_3.
58. Singh R, Cao W, Al-Naib I, Cong L, Withayachumnankul W, Zhang W (2014) Ultrasensitive terahertz sensing with high- Q Fano resonances in metasurfaces. Appl. Phys. Lett. 105(17). https://doi.org/10.1063/1.4895595
59. Almawgani AHM et al (2023) A Graphene-Metasurface-Inspired Optical Sensor for the Heavy Metals Detection for Efficient and Rapid Water Treatment. Photonics 10(1). https://doi.org/10.3390/photonics10010056
60. S. Raj, S. Patle, and S. Rajendran, "Predicting crop yield using decision tree regressor," in IEEE International Conference on Knowledge Engineering and Communication Systems, ICKES 2022, 2022. doi: https://doi.org/10.1109/ICKECS56523.2022.10060730.
61. Scikit-learn, "Decision tree regressor," Scikit-learn.
62. Luo H, Cheng F, Yu H, Yi Y (2021) SDTR: soft decision tree regressor for tabular data. IEEE Access 9:55999–56011. https://doi.org/10.1109/ACCESS.2021.3070575
63. M. Zenga and C. Colapinto, "Decision tree for classification and forecasting," in Engineering Mathematics and Artificial

Intelligence: Foundations, Methods, and Applications, 2023, pp. 53–81. doi: https://doi.org/10.1201/9781003283980-3.
64. Gulati P, Sharma A, Gupta M (2016) Theoretical study of decision tree algorithms to identify pivotal factors for performance improvement: a review. Int J Comput Appl 141(14):19–25. https://doi.org/10.5120/ijca2016909926